日本磁気学会
ISSN 2432-0250
Journal of the Magnetics Society of Japan
Electronic Journal URL: https://www.jstage.jst.go.jp/browse/msjmag

Vol.45 No.2　2021

Journal

JOURNAL OF THE MAGNETICS SOCIETY OF JAPAN

Vol.45 No.2 2021

日本磁気学会

ISSN 2432-0250

HP: http://www.magnetics.jp/ e-mail: msj@bj.wakwak.com
Electronic Journal: http://www.jstage.jst.go.jp/browse/msjmag

世界初！
高温超電導型VSM

新製品

世界初*、高温超電導マグネットをVSMに採用することで
測定速度 当社従来機1/20を実現。
0.5mm cube磁石のBr, HcJ高精度測定が可能と
なりました。
*2014年7月 東英工業調べ

測定結果例

高温超電導VSMによるNdFeB(sint.) 0.5mm cube BHカーブ

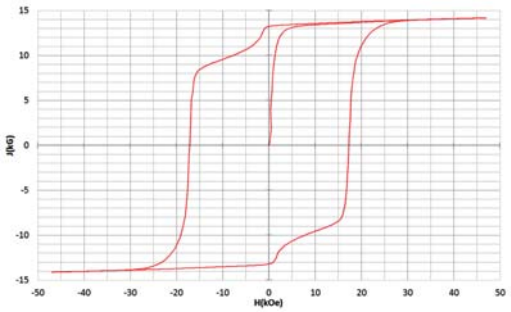

磁化測定レンジ：0.2emu
Br = 13.2kG　　HcJ = 17.2kOe

高温超電導VSMによるNdFeB(sint.) 1mm cube BHカーブ

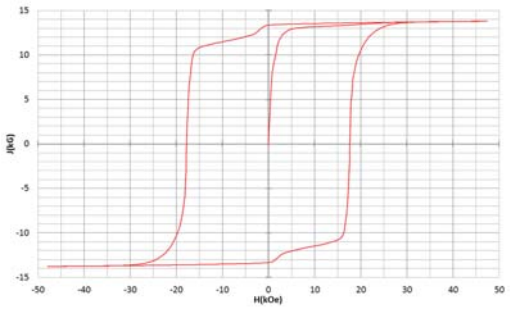

磁化測定レンジ：2emu
Br = 13.3kG　　HcJ = 17.7kOe

高温超電導VSMによるNdFeB(sint.) 4mm cube BHカーブ

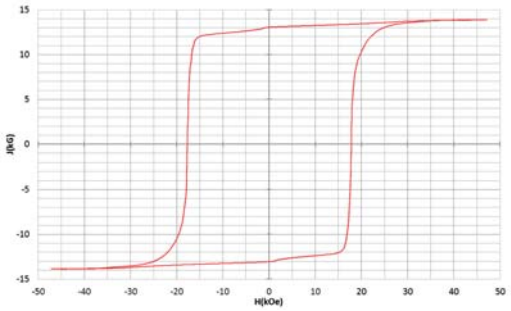

磁化測定レンジ：100emu
Br = 13.1kG　　HcJ = 17.8kOe

高速測定を実現

高温超電導マグネット採用により、高速測定を実現しました。Hmax= 5Tesla, Full Loop 測定が2分で可能です。
（当社従来機：Full Loop測定　40分）

小試料のBr,HcJ高精度測定

0.5mm cube 磁石のBr,HcJ高精度測定ができ、表面改質領域を切り出しBr,HcJの強度分布等、微小変化量の比較測定が可能です。
また、試料の加工劣化の比較測定が可能です。

試料温度可変測定

−50℃～+200℃温度可変UNIT（オプション）

磁界発生部の小型化

マグネットシステム部寸法：0.8m×0.3m×0.3m

TOEI 東英工業株式会社
http://www.toeikogyo.co.jp
〒194-0035 東京都町田市忠生1-8-13
TEL：042-791-1211 FAX：042-792-0490
E-mail : sales@toeikogyo.co.jp

Journal of the Magnetics Society of Japan
Vol. 45, No. 2

Electronic Journal URL: https://www.jstage.jst.go.jp/browse/msjmag

CONTENTS

J. Magn. Soc. Jpn., **45**, 12-15 (2021)

<Review>

Miniaturized Permanent Magnets Applied to Extremely Small Stepping Motors

Masaki Nakano

Graduate School of Engineering, Nagasaki University, *1-14 Bunkyo-machi, Nagasaki, Nagasaki 852-8521, Japan*

This is a review paper on the fabrication of Pr-Fe-B thin magnets using a PLD (Pulsed Laser Deposition) method. It is generally known that conventional isotropic Nd-Fe-B bonded magnets including resin have been used for small motors such as stepping motors. In this study, Pr-Fe-B magnet powders without resin were consolidated on a small shaft obtain a small magnet instead of a bonded magnet. After annealing the as-deposited sample, multi-pole magnetization was carried out for the sample using a micro-magnetization process. As a result, the stable operation of an ultra-small stepping motor with a diameter less than 3.0 mm that contained the above-mentioned magnet was demonstrated. It was confirmed that the size of stepping motors could be further reduced in the study.

Key words: Pr-Fe-B magnet, PLD (Pulsed Laser Deposition), micro-magnetization, stepping motor

1. Introduction

Several researchers have reported the size reduction of a motor equipped with miniaturized permanent magnets. In 1991, Yamashita and Yamasaki prepared a milli-size motor containing a sputtering-made Nd-Fe-B thin-film magnet[1]. Our group demonstrated an axial gap type DC brushless motor with thickness of 0.8 mm and outer diameter of 5 mm. In the motor, a 0.2 -mm-thick Nd-Fe-B film magnet fabricated by a PLD[2] was applied. A DC brush-less micro-motor was also reported by Machida *et al.* through improving the magnetic properties of a small-sized Nd-Fe-B bulk magnet[3]. In the case of a miniaturized nano-composite magnet, the consolidation of α-Fe/$Pr_2Fe_{14}B$-based thick-films enabled us to enhance the magnetic torque of cylindrical micro rotors[4]. In addition, Shinshi *et al.*[5] demonstrated a MEMS (Micro Electro Mechanical Systems) linear motor utilizing a thin film permanent magnet deposited on a Si substrate through sputtering.

Here, the size reduction of a stepping motor was focused on[6][7]. Rare earth-based bonded magnets have been widely used in commercial small motors including stepping motors. However, it is difficult to enhance the values of residual magnetic polarization and $(BH)_{max}$ because of the existence of non-magnetic material such as thermosetting resin in the magnets. We, therefore, consolidated permanent magnet powders without resin by utilizing the PLD method. Considering the demagnetization field due to the structure of the desired small motor, we need to increase the coercivity up to 1000 kA/m, the reson being that the permeance coefficient in the demagnetization curve is estimated at 1.0. Since the magnetic crystalline anisotropy constant of a $Pr_2Fe_{14}B$ phase (K_u = 6.8 MJ/m^3) is larger by approximately 2.3 MJ/m^3 when compared with a $Nd_2Fe_{14}B$ phase (K_u = 4.5 MJ/m^3)[8], Pr-Fe-B thick-film magnets were chosen over Nd-Fe-B thick films.

In this study, Pr-Fe-B magnet powders with a coercivity (H_{cj}) exceeding 1000 kA/m were deposited on a thin stainless shaft using the PLD method. Furthermore, an extremely small stepping motor containing the above-mentioned Pr-Fe-B magnet with multi-pole magnetization was demonstrated.

2. Experimental

A $Pr_XFe_{14}B$ (X = 1.6~2.4) target was ablated with a Nd-YAG pulse laser (wavelength: 355 nm) at a repetition rate of 30 Hz in a vacuum. The laser power was approximately 4 W. Before the ablation, the chamber was evacuated down to about 2.0~4.0×10^{-5} Pa by using a rotary pump together with a molecular turbo pump. The distance between the target and stainless plate used in the chamber was fixed at 10 mm. The area of all films obtained on the stainless plates was 5×5 mm^2. The average deposition rate exceeded approximately 40 μm/h. In the case of the stainless shaft, the distance between the target and shaft, which had a diameter of approximately 0.75 mm, was fixed at 5 mm. The deposition was carried out using eight different positions to surround a film on the shaft. Pr-Fe-B film could be made to cover the whole shaft by repeating the deposition eight times. Pulse annealing (PA) [9] was carried out to crystallize the films because all the films, as-deposited, had an amorphous structure.

After the annealing process, samples were magnetized up to 7 T with a pulse magnetizer. Hysteresis loops were measured with a VSM (Vibrating Sample Magnetometer) which could apply a magnetic field up to approximately 2000 kA/m reversibly. The in-plane magnetic field was applied for the stainless plate. In the case of the stainless shaft, the magnetic field was applied in the longitudinal direction. The composition of the obtained films was evaluated with SEM (Scanning Electron Microscope)-EDX (Energy Dispersive X-ray spectrometry), and the surface was also observed by using a SEM. The average thickness was measured with a micrometer or estimated by measuring each weight.

The Pr-Fe-B thin magnets on the shaft were polished to obtain a smooth surface and then micro-magnetized.

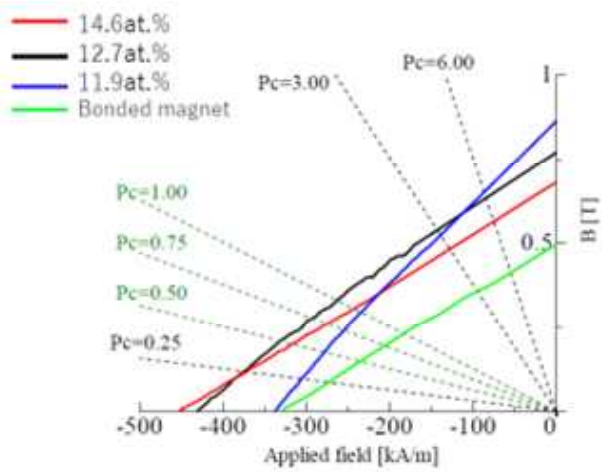

Fig. 1 2nd quadrant of *B*-*H* curves of three Pr-Fe-B film magnets with different Pr contents and conventional Nd-Fe-B bonded magnet.

Multipole magnetization was carried out as follows[10]. To adjust the magnetization characteristics, the Pr-Fe-B magnets were thermally magnetized. After rapidly heating the Pr-Fe-B magnets to temperatures above the Curie point in the air, they were cooling it in the magnetizing field of permanent magnets. Sm-Co sintered magnets were used to facilitate magnetization, and a heater in the magnetizing area was prepared. The above-mentioned micro-magnetization equipment enabled us to obtain 10 magnetic poles per magnet. Each thin magnet with multi-pole magnetization was loaded in a stepping motor with a diameter of 2.9 mm, and the operation of the motor was observed by using a conventional test device (MCH-5B, NPM Corporation).

3. Results and Discussions

We have already reported the preparation of Pr-Fe-B film magnets with $H_{cj} \geqq 1000$ kA/m in the reference 7). Figure 1 shows the 2nd quadrant of the *B*-*H* curves of three Pr-Fe-B film magnets with different Pr contents on stainless plates and conventional Nd-Fe-B bonded magnets. The 350-μm-thick conventional bonded magnets[6] (H_{cj} : 740 kA/m, J_r : 0.6 T) have been used in commercial stepping motors. Two of the Pr-Fe-B films with Pr contents [Pr/(Pr+Fe)] of 12.7 and 14.6 at.% showed superior values of coercivity (H_{cB}) and residual magnetic induction (B_r) compared with those of the bonded magnet. We evaluated the values of the energy product [*(BH)*] at $P_c = 1.0$ as a function of rare earth (Pr or Nd) content in the Pr-Fe-B film magnets on stainless plates. (see Fig. 2) Here, the values of the conventional Nd-Fe-B bonded magnets are indicated. It was clarified that the *(BH)* values of almost all the Pr-Fe-B films were higher than those of the Nd-Fe-B bonded magnets. Examination on the mechanical characteristics of applying the above-mentioned Pr-Fe-B films to a stepping motor revealed that films, as-deposited with a Pr content above 15 at.%, peeled off from the stainless

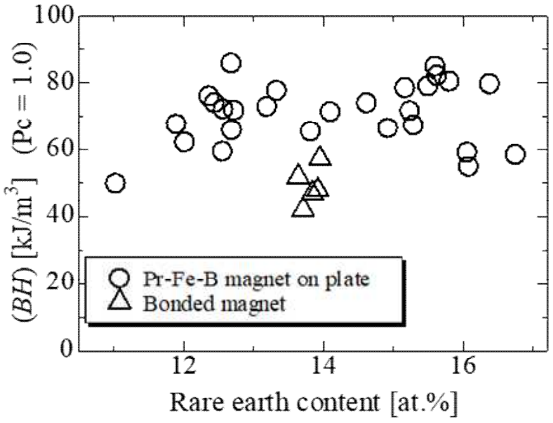

Fig. 2 Energy product [*(BH)*] at permeance coefficient of 1.0 as function of rare earth content on PLD-made Pr-Fe-B film magnets and conventional Nd-Fe-B bonded magnets.

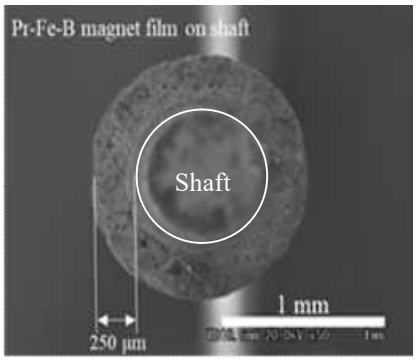

Fig. 3 Cross-sectional view of Pr-Fe-B thin magnet deposited on thin stainless shaft. Surface of magnet was polished to obtain uniform thickness of approximately 250 μm.

plates. We suppose that the peeling phenomenon occurred due to the different values of each linear expansion coefficient of the stainless plate (10.3×10^{-6} K^{-1}) and Pr element (6.7×10^{-6} K^{-1}). It was found that controlling the Pr content is indispensable when trying to achieve not only high coercivity but also an increase in thickness without mechanical destruction such as peeling.

Figure 3 shows photographs of an approximately 250-μm-thick Pr-Fe-B magnet after polishing the surface. Judging from the cross-sectional photo, it was confirmed that the thin magnet uniformly surrounded the shaft. Moreover, the influence of thermal damage in the air during micro-magnetization was evaluated. Figure 4 shows each value of the energy product [*(BH)*] at P_c = 1.0 of five Pr-Fe-B thin magnets with different Pr contents crystallized through rapid heating in the air without a magnetic field. The heating temperature exceeded 620 K, which is higher than the Curie temperature of the $Pr_2Fe_{14}B$ magnetic phase (569 K). The heating process in the air did not degrade the

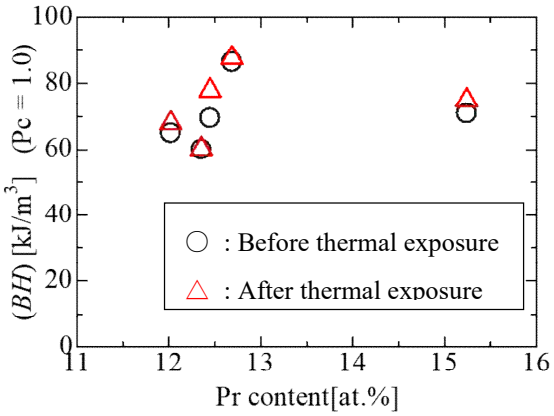

Fig. 4 Comparison of values of energy product [*(BH)*] at P_c = 1.0 before and after thermal exposure at temperature above 630 K in air without magnetic field. Here, Pr-Fe-B thin magnets with various Pr contents were prepared.

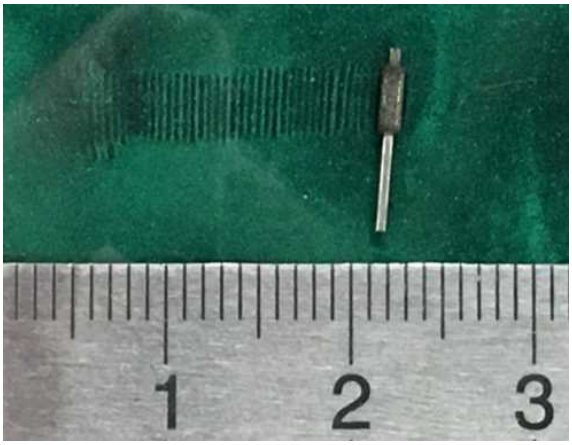

Fig. 5 Micro-magnetized Pr-Fe-B magnet on magnetic view sheet (product name). We confirmed multi-pole magnetization using micro-magnetization through rapid annealing and cooling process.

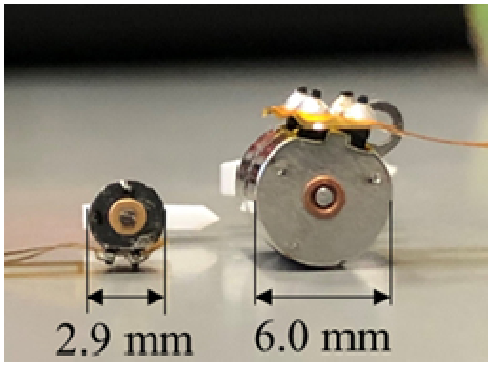

Fig. 6 Two stepping motors containing 250-μm-thick Pr-Fe-B thin magnet and Nd-Fe-B bonded magnet, respectively. Reduction in size could be achieved by using PLD-made thin magnet.

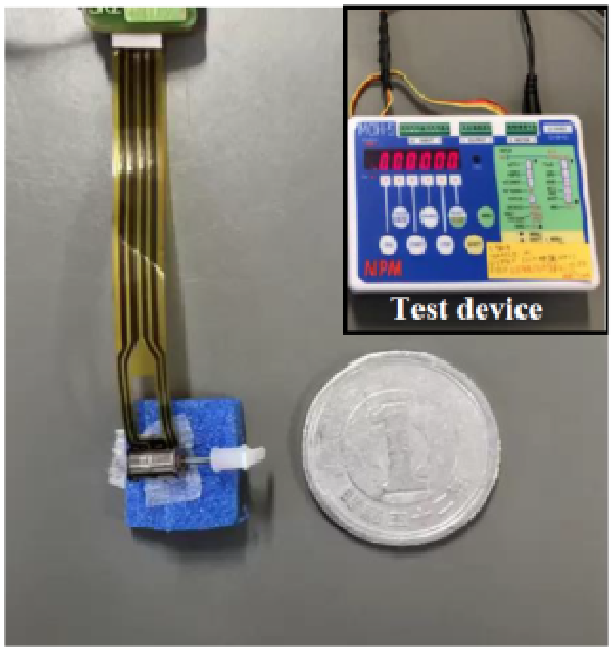

Fig. 7 Test device (inset) for evaluating performance of an ultra-small stepping motor. Stable operation of the stepping motor with a diameter less than 3.0 mm was demonstrated.

energy product of any of the samples. Then, multipole magnetization for the above-mentioned Pr-Fe-B isotropic magnets was carried out. The magnetization characteristic of the sample seen in Fig. 3 was observed (see Fig. 5). A magnetic pattern was drawn on a magnetic view sheet (Product name) by rolling the sample. We, therefore, assembled a small stepping motor using the micro-magnetized Pr-Fe-B thin magnet. Figure 6 shows a stepping motor with a diameter of 2.9 mm containing the PLD made magnet. A conventional stepping motor including a Nd-Fe-B bonded magnet is also shown. At present, it was difficult to measure the motor performance on the basis of concrete physical (mechanical) values due to the ultimately small value. Instead, as displayed in Fig. 7, the motor performance was observed using a conventional test device that enabled us to set the rotation direction, speed control, position control, operation mode, and stop time of the stepping motor. Here, another conventional motor (diameter: 4.3 mm) including a Nd-Fe-B bonded magnet was also used. We confirmed that the operational stability of the ultra-small stepping motor was comparable with that of commercial motors.

4. Summary

The utilization of PLD-made Pr-Fe-B thin magnets enabled us to prepare an ultimately small stepping motor with stable operation. In the future, the motors with the diameter less than 3 mm are expected to be applied in various fields such as medical devices.

Acknowledgements

The author would like to express the deepest gratitude to Dr. Fukunaga (Emeritus professor of Nagasaki university), Prof. Yanai (Nagasaki university) and Dr. Yamashita (Nagasaki university) for their helpful discussion and suggestions. Thanks are also due to Mr. Takeichi as a graduate course student in Nagasaki university for experimental data. Moreover, the author is indebted to Mr. Komura and Mr. Okawara (MinebeaMitsumi Inc.) for the preparation of stepping motors. This work was also supported by the JSPS KAKENHI under Grant JP 19H02173 and 19H00738.

References

1) S. Yamashita and J. Yamasaki: *J. Appl. Phys.,* **70**, 6627 (1991).
2) M. Nakano, S. Sato, F. Yamashita, T. Honda, J. Yamasaki, K. Ishiyama, M. Itakura, J. Fiedler, T.Yanai and H. Fukunaga: *IEEE Trans. Mag.,* **43**, 2672 (2007).
3) K. Machida, S. Suzuki, K. Ishigaki, T. Kukita, E. Sakaguchi, T. Kitamori, Y. Shimizu, K. Nakamura, and
4) F. Yamashita, S. Nishimura, O. Kobayashi, M. Itoh, M. Nakano, H. Fukunaga and K. Ishiyama: *J. Appl. Phys.* E. Fukushima: *Report of No. 142 Technical Meeting of MSJ (The Magnetics Society of Japan)*, 25 (2005). **109**, 07A712 (2011).
5) R. Fujiwara, T. Shinshi, and M. Uehara: *International Journal of Automation Technology,* **7**, 148 (2013).
6) M. Nakano, S. Takeichi, K. Takashima, A. Yamashita, T. Yanai, and H. Fukunaga: *IEEE Trans. Magn,* **56**, 7516303 (2020).
7) M. Nakano, S. Takeichi, K. Inoue, K. Takashima, A. Yamashita, T. Yanai, and H. Fukunaga: *AIP advances*, **10**, 015030 (2020).
8) K. H. J. Buschow, *Handbook of Ferromagnetic Materials*, 4 (1988).
9) H. Fukunaga, K. Tokunaga, and J. Man Song: *IEEE Trans. Magn.*, 38, 2970 (2002).
10) H. Komura, M. Kitaoka, T. Kiyomiya, and Y. Matsuo: *IEEE Trans. Magn*, 44, 4266 (2008).

Received Oct. 04, 2020, Accepted Dec. 24, 12, 2020.

J. Magn. Soc. Jpn., **45**, 16-24 (2021)

<Paper>

Medium Layer Structure in Three-Dimensional Heat-Assisted Magnetic Recording

T. Kobayashi, Y. Nakatani*, and Y. Fujiwara

Graduate School of Engineering, Mie Univ., *1577 Kurimamachiya-cho, Tsu 514-8507, Japan*

*Graduate School of Informatics and Engineering, Univ. of Electro-Communications, *1-5-1 Chofugaoka, Chofu 182-8585, Japan*

We examine a medium layer structure in three-dimensional heat-assisted magnetic recording (3D HAMR) at 2 Tbpsi per layer (total density of 4 Tbpsi) where the medium consists of a high Curie temperature (HC) layer and a low Curie temperature (LC) layer. We perform a heat transfer simulation for 3D HAMR media including the isolation layer. To evaluate the grain error distribution, the expected value of the magnetization is calculated using the grain error probability. The error threshold and the time dependence of the bit error rate are discussed for 10 years of archiving. The information stability in the HC layer while writing in the LC layer is estimated using the temperature profile calculated by the heat transfer simulation. An LC (upper, namely, surface) / HC (lower) layer structure is compared with an HC (upper) / LC (lower) layer structure. The former is disadvantageous in relation to the medium surface temperature as regards writing in the HC layer. The latter may be disadvantageous in relation to the difference between the thermal gradients for HC and LC writing.

Key words: 3D HAMR, heat transfer simulation, temperature profile, information stability, error distribution

1. Introduction

Microwave-assisted magnetic recording (MAMR), heat-assisted magnetic recording (HAMR), and three-dimensional magnetic recording are candidates as next generation magnetic recording methods for achieving a high recording capacity. HAMR is a recording technique where the medium is heated to reduce coercivity during the writing period.

Three-dimensional HAMR (3D HAMR) has been proposed[1] where the medium consists of a high Curie temperature T_{HC} (HC) layer and a low Curie temperature T_{LC} (LC) layer with an isolation layer inserted between the two layers to suppress exchange coupling between them. With 3D HAMR, once data have been written in the HC layer, other data can be written in the LC layer by employing lower temperature heating.

We have previously discussed the information stability in the HC and LC layers for 10 years of archiving, and the stability of the information in the HC layer while writing is under way in the LC layer[2]. We have also discussed 3D HAMR media design[3]. We used these results to roughly determine the preferable layer structure for 3D HAMR, namely an LC (upper, namely, surface) / HC (lower) layer, where the LC layer has a T_{LC} of 625 K and a layer thickness h_{LC} of 4.5 nm, and the HC layer has a T_{HC} of 750 K and an h_{HC} of 6.0 nm. However, we analytically estimated the temperature profile in it using previously published data where the recording layer thickness was 8.0 nm without the isolation layer.

In this paper, we carry out a heat transfer simulation for 3D HAMR media where the recording layer thickness is 11.5 nm including an isolation layer of 1.0 nm. To evaluate the grain error distribution, the expected value of the magnetization is calculated using the grain error probability. We discuss both the error threshold and the time dependence of the bit error rate for 10 years of archiving. We then estimate the information stability in the HC layer while writing in the LC layer using a temperature profile calculated by using a heat transfer simulation. Furthermore, we examine two layer structures consisting of an LC / HC layer and an HC / LC layer.

2. Calculation Method

2.1 Magnetic properties

The temperature dependence of the magnetization M_s was calculated by employing a mean field analysis[4], and that of the anisotropy constant K_u was assumed to be proportional to M_s^2[5]. $M_s(T_c, T)$ is a function of the Curie temperature T_c and temperature T. And $M_s(T_c = 770\ \mathrm{K}, T = 300\ \mathrm{K}) = 1000\ \mathrm{emu/cm^3}$ was assumed for FePt.

We introduced an HAMR design parameter, namely, the medium anisotropy constant ratio K_u/K_{bulk}[6] since the K_u value is a function of T_c. K_u/K_{bulk} is the intrinsic ratio of the medium K_u to bulk FePt K_u regardless of T_c. Although a low T_c medium is easy to write when employing HAMR, a high K_u/K_{bulk} is needed for a low T_c medium for 10 years of archiving[7], and a medium with a high K_u/K_{bulk} is difficult to manufacture regardless of T_c[8]. Moreover, a high K_u/K_{bulk} must be achieved in 3D HAMR to realize information stability in the LC layer for 10 years of archiving, and to realize information stability in the HC layer while writing in the LC layer[2]. $K_u(T_c, K_u/K_{bulk}, T)$ is a function of T_c, K_u/K_{bulk}, and T. And $K_u(T_c = 770\ \mathrm{K}, K_u/K_{bulk} = 1, T = 300\ \mathrm{K}) = 70\ \mathrm{Merg/cm^3}$ was assumed for bulk FePt. We used $K_u/K_{bulk} = 0.8$ in this paper.

The T_c value can be adjusted by adjusting the Cu composition z for $(Fe_{0.5}Pt_{0.5})_{1-z}Cu_z$.

2.2 Field strength

We assumed the medium to be granular and the recording density to be 2 Tbpsi per layer (total density of 4 Tbpsi). The magnetic field strength from the upper and lower layers, as shown in Fig. 1, was calculated using an analytical equation. One bit has m = 3 grains for the cross-track direction and n = 3 grains for the down-track direction, namely, there are $m \times n$ = 9 grains/bit. The bit aspect ratio is one. The grain size D_m and the intergrain spacing Δ_G are 5.0 nm and 1.0 nm, respectively, with no grain size distribution. The grain heights (layer thicknesses) and the magnetizations for the upper and lower layers are h_U, h_L, M_{sU}, and M_{sL}, respectively. The flying height h_{fly} = 4.0 nm is the distance between the magnetic head reader and the upper layer surface.

The isolation layer is used to suppress the exchange coupling between the upper and lower layers. That layer thickness h_{Iso} must be thinner due to the higher field strength from the lower layer at the reader since the field strength decreases exponentially with an $h_{fly} + h_U + h_{Iso}$ value of more than 3 nm[3]. On the assumption that we had selected an appropriate material for the isolation layer, we chose an h_{Iso} value of 1.0 nm.

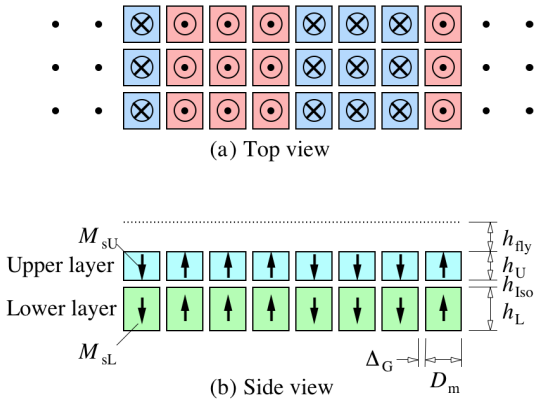

Fig. 1 Grain arrangement for field calculation. (a) Top and (b) side views.

2.3 Temperature profile

We needed to determine the temperature profiles of the LC and HC layers at the time of writing for the 3D HAMR design. A heat transfer simulation was carried out using Poynting for Optics (Fujitsu Ltd.). Figure 2 shows a schematic illustration of the structure of a medium that consists of four layers, namely, a recording layer (RL) (FePt base, upper + isolation + lower layers = 11.5 nm), interlayer 1 (IL1) (MgO base, 5 nm), interlayer 2 (IL2) (Cr base, 10 nm), and a heat-sink layer (Cu base, 30 nm). Since suitable intergrain and isolation layer materials are currently unknown, we used the optical and thermal constants of FePt for these materials. The total layer thickness of the LC and HC layers was 11.5 − 1.0 = 10.5 nm. IL1 is a layer for the c-axis orientation control of RL, and IL2 is a seed layer for IL1. The x, y, and z axes are the down-track, cross-track, and film normal directions, respectively, where y = 0 at the track center and z = 0 at the RL surface. The writing temperature of the grains at the track edges $y = \pm 6.0$ nm was assumed to be $T_{cm} + 2\sigma_{Tc}$ for the HC and LC layers where T_{cm} and σ_{Tc} are the mean Curie temperature and the standard deviation of T_{cm}, respectively, taking account of the Curie temperature variation.

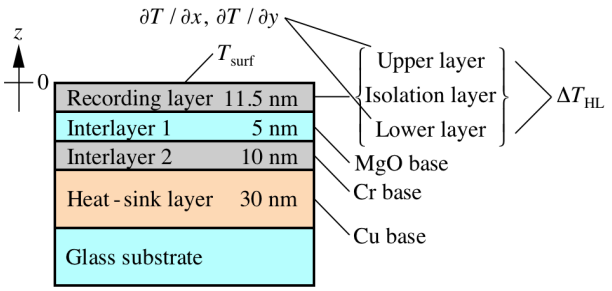

Fig. 2 Medium structure for heat transfer simulation.

Table 1 (a) Calculation conditions, (b) optical constants, and (c) thermal constants for heat transfer simulation.

(a)

Wavelength λ (nm)	780
Light-spot diameter D_L (nm)	9.0 (FWHM)
Linear velocity v (m/s)	10
Ambient temperature T_{amb} (K)	330

(b)

	Refractive index	Extinction coefficient
Recording layer	3	4
Interlayer 1	1.73	0
Interlayer 2	4.11	4.35
Heat-sink layer	0.242	4.85
Glass substrate	1.5	0

(c)

	Specific heat	Thermal conductivity
Recording layer	200 J/(kgK) 3 J/(cm^{3}K)	100 W/(mK)
Interlayer 1	500 J/(kgK) 2 J/(cm^{3}K)	4 W/(mK)
Interlayer 2	360 J/(kgK) 2.5 J/(cm^{3}K)	100 W/(mK)
Heat-sink layer	440 J/(kgK) 4 J/(cm^{3}K)	400 W/(mK)
Glass substrate	1000 J/(kgK) 2 J/(cm^{3}K)	1 W/(mK)

We focused on the medium surface temperature T_{surf} while writing in the HC layer, the thermal gradients for the down-track $\partial T/\partial x$ and cross-track $\partial T/\partial y$ directions while writing in the LC and HC layers, and the grain temperature difference ΔT_{HL} between the HC and LC layers while writing in the LC layer at the track edges $y = \pm 6.0$ nm.

Table 1 summarizes (a) calculation conditions, (b) optical constants, and (c) thermal constants used in the simulation. The light spot diameter (FWHM) is about 9.0 nm for the down-track and cross-track directions. The linear velocity is 10 m/s. The ambient temperature is the maximum working temperature of the hard disk drive, and is assumed to be 330 K.

2.4 Information stability

The information stability in 3D HAMR was estimated using the grain error probability P[2], taking account of the shape anisotropy $M_s H_d/2$ using a self-demagnetizing field H_d [3]. The conditions used when calculating the information stability in the LC and HC layers are summarized in Table 2.

We assumed that the grain size distribution was log-normal with a mean grain size D_m of 5.0 nm and a standard deviation σ_D/D_m of 15 %. The T_c distribution was assumed to be normal with a mean Curie temperature T_{cm} and a standard deviation σ_{Tc}/T_{cm} of 2 %. No intrinsic distribution of K_u was assumed. However, there was a fluctuation in K_u caused by σ_{Tc}.

The result calculated with a heat transfer simulation in **2.3** was used as the temperature profile for the cross-track direction while writing in the LC layer.

To evaluate the grain error distribution, we calculated the expected value of the magnetization $E[M_s]$

$$E[M_s] = (1-P)M_s + P(-M_s) = (1-2P)M_s. \quad (1)$$

The $E[M_s]$ value was averaged over one-bit grains ($m \times n = 9$) to give the information stability during 10 years of archiving,

$$E[M_s] = \frac{\sum_{i=1}^{m}\sum_{j=1}^{n}(1-2P_{ij})M_{sij}(T_{cij},\ 330\ \mathrm{K})}{m \times n}, \quad (2)$$

and was averaged over one-row grains ($n = 3$) for the information stability in the HC layer while writing in the LC layer,

$$E[M_{si}] = \frac{\sum_{j=1}^{n}(1-2P_{ij})M_{sij}(T_{cij},\ 330\ \mathrm{K})}{n}, \quad (3)$$

since there is a temperature distribution for the cross-track direction.

Furthermore, we introduced an error threshold E_{th} to estimate the bit error rate (bER). Errors occur in some grains of a bit. We assume that if the ratio of the surface magnetic charge $\sum_{i,j} M_{sij}(T_{cij},\ 330\ \mathrm{K})D_{ij}^2$ of the grains where the magnetization turns in the recording direction to the total surface magnetic charge $(m \times n)M_s(T_{cm},\ 330\ \mathrm{K})D_m^2$ in a bit is more than E_{th}, namely,

$$\frac{\sum_{i,j} M_{sij}(T_{cij},\ 330\ \mathrm{K})D_{ij}^2}{(m \times n)M_s(T_{cm},\ 330\ \mathrm{K})D_m^2} > E_{th}, \quad (4)$$

the bit is error free where M_{sij}, T_{cij}, and D_{ij} are the magnetization, the Curie temperature, and the grain size of the ij-th grain, respectively.

The readout magnetic field at the reader will be degraded after 10 years of archiving or writing in the LC layer. The lowest normalized magnetic field H_0 that must be readable without error can roughly be represented by E_{th} as

$$H_0 = 2E_{th} - 1. \quad (5)$$

Table 2 Calculation conditions for information stability.

Recording density (Tbpsi / layer)	2
Total density (Tbpsi)	4
Grain number $m \times n$ (grains / bit)	3 × 3
Intergrain spacing Δ_G (nm)	1.0
Mean grain size D_m (nm)	5.0
Standard deviation σ_D / D_m (%) of D_m	15
Bit pitch D_B (nm)	18.0
Track width D_T (nm)	18.0
Bit aspect ratio D_T / D_B	1.0
Standard deviation σ_{Tc} / T_{cm} (%) of T_{cm}	2
Anisotropy constant ratio K_u / K_{bulk}	0.8
Gilbert damping constant α	0.1

3. Calculation Results

3.1 LC / HC layer structure

First, we discuss the structure as shown in Fig. 3 (a) where the upper layer is LC with T_{LC} = 650 K and h_{LC} = 4.5 nm, and the lower is HC with T_{HC} = 750 K and h_{HC} = 6.0 nm. The T_{LC} value was revised to 650 from 625 K in a previous paper[3] due to information stability in the LC layer during 10 years of archiving.

Figure 3 (b) shows the z component H_z of the magnetic field at the track center and the reader position from the LC and HC layers for the down-track direction using 3 grains for the cross-track direction. The peak z component H_{zpeak} values are 1151 and 570 Oe from the LC and HC layers, respectively, where h_{fly} is 4.0 nm.

3.1.1 Temperature profile

Figure 4 shows the temperature profiles calculated employing a heat transfer simulation for the cross-track direction. The solid lines indicate the temperatures at the layer boundaries, and the dotted lines indicate those at the layer centers.

(a) When writing in the LC layer (LC writing), the temperature at $y = \pm 6.0$ nm and $z = -2.25$ nm is $T_{LC} + 2\sigma_{TLC}$ = 676 K at which $\partial T_L/\partial y$ is 12.0 K/nm. The ΔT_{HL} value is −42 K.

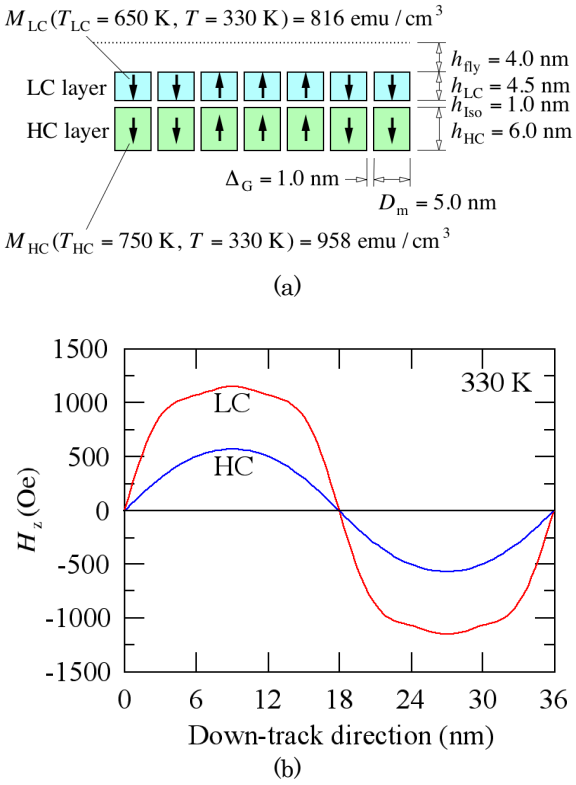

Fig. 3 (a) Layer structure for LC / HC and (b) field strength H_z from LC and HC layers for the down-track direction.

(b) When writing in the HC layer (HC writing), the temperature at $y = \pm 6.0$ nm and $z = -8.5$ nm is $T_{HC} + 2\sigma_{THC} = 780$ K at which $\partial T_H/\partial y$ is 9.0 K/nm. The T_{surf} value is 957 K. It should be noted that the temperature of the LC layer ($z = -2.25$ nm) in the center of adjacent tracks ($y = \pm 18.0$ nm) is 671 K, which is higher than T_{LC}, and HC writing will erase the data of the LC layer in the adjacent tracks. Therefore, it is necessary to devise a suitable writing method to address this issue, *e.g.* combination with shingled magnetic recording.

The results obtained for $T_{HC} = 750$ K are summarized in Table 3 (a). The T_{surf} value of 957 K is relatively high since HC is the lower layer. This is disadvantageous in terms of the heat resistance of the writing head and/or the surface lubricant.

We have reported as regards the thermal gradient in 3D HAMR[3]:

(1) The thermal gradient for the upper layer is intrinsically larger than that for the lower layer due to a heat flow in the in-plane direction in the deep part of the layer.

(2) The thermal gradient for the HC layer is intrinsically larger than that for the LC layer due to their respective Curie temperatures.

The difference between the thermal gradients for LC and HC writing is relatively small due to the combinations of the upper LC layer and the lower HC layer.

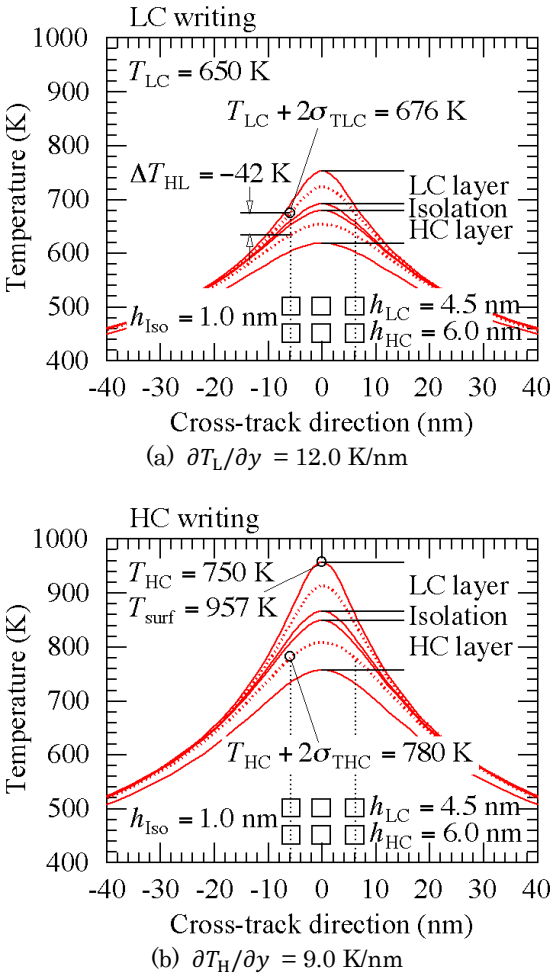

Fig. 4 Temperature profile in the cross-track direction for an LC (upper) / HC (lower) layer structure while writing in the (a) LC and (b) HC layers.

The ΔT_{HL} value of -42 K is negative, which means that the temperature in the HC layer while writing in the LC layer is lower than that in the LC layer, and this is advantageous in relation to the information stability in the HC layer.

By reducing T_{HC}, T_{surf} can be reduced. Furthermore, the heating power P_w can also be reduced. The results for $T_{HC} = 725$ K are summarized in Table 3 (b). In comparison with the result for $T_{HC} = 750$ K, T_{surf} is reduced to 920 from 957 K and P_w can be reduced to 0.94.

3.1.2 Information stability for 10 years of archiving

We estimated the information stability for 10 years of archiving with no writing field H_w using the grain error probability. The storage temperature is 350 K since we take a certain margin for temperature into account. The calculation bit number was 1E+7. The allowable bER is assumed to be 1E−3.

Table 3 Results of heat transfer simulation for LC / HC layer structure ((a) T_{HC} = 750 and (b) 725 K).

(a)

	LC writing	HC writing
LC / HC layer structure		
T_{cm} (K)	650	750
h (nm)	4.5	6.0
T_{surf} (K)		957
$\partial T / \partial x$ (K / nm)	12.2	8.9
$\partial T / \partial y$ (K / nm)	12.0	9.0
ΔT_{HL} (K)	–42	

(b)

	LC writing	HC writing
LC / HC layer structure		
T_{cm} (K)	650	725
h (nm)	4.5	6.0
T_{surf} (K)		920
$\partial T / \partial x$ (K / nm)	12.2	8.4
$\partial T / \partial y$ (K / nm)	12.0	8.4
ΔT_{HL} (K)	–42	
$P_w / P_w (T_{HC} = 750\ K)$		0.94

Grain error distributions are shown in Figs. 5 (a) LC and (b) HC layers for 10 and 0.001 yrs where 0.001 yrs corresponds to about 9 hrs. The peaks in the figures represent grain error, and the $E[M_s]$ value is negative for 5 or more grain errors since the total grain number is nine. For (a) the LC layer, 3 grain errors can be seen even after 0.001 yrs, and 5 grain errors will occur after 10 yrs since the LC layer has a low Curie temperature and a thin layer. For (b) the HC layer, only 1 grain error can be seen after both 0.001 and 10 yrs due to a high Curie temperature and a thick layer.

Figure 6 shows bER as a function of E_{th} for 10 years of archiving. The second horizontal axis is the lowest H_0 value that must be readable without error, which was estimated using Eq. (5). E_{th} values of 0.581 and 0.744 are required for the LC and HC layers, respectively.

The information will be degraded in the LC layer and it will be scarcely degraded in the HC layers as shown in Fig. 5. Figure 7 shows time dependence of bER. Errors increase over time in the LC layer, and the error does not increase in the HC layer with both T_{HC} = 750 K and 725 K (not shown). The bit error rate bER_{10} after 10 years of archiving is expressed as

$$bER_{10} = bER_{ini} + \Delta bER, \qquad (6)$$

where bER_{ini} and ΔbER are the initial bit error rate before archiving and the increase in the bit error rate during archiving, respectively. For the LC layer, ΔbER is about 1E−3 for E_{th} = 0.581. Therefore, bER_{ini} must be low, for example, 1E−4. In this case, bER_{10} will be 1.1E−3. On the other hand, bER_{ini} = 1E−3 is allowable for the HC layer since there was no change in bER over ten years.

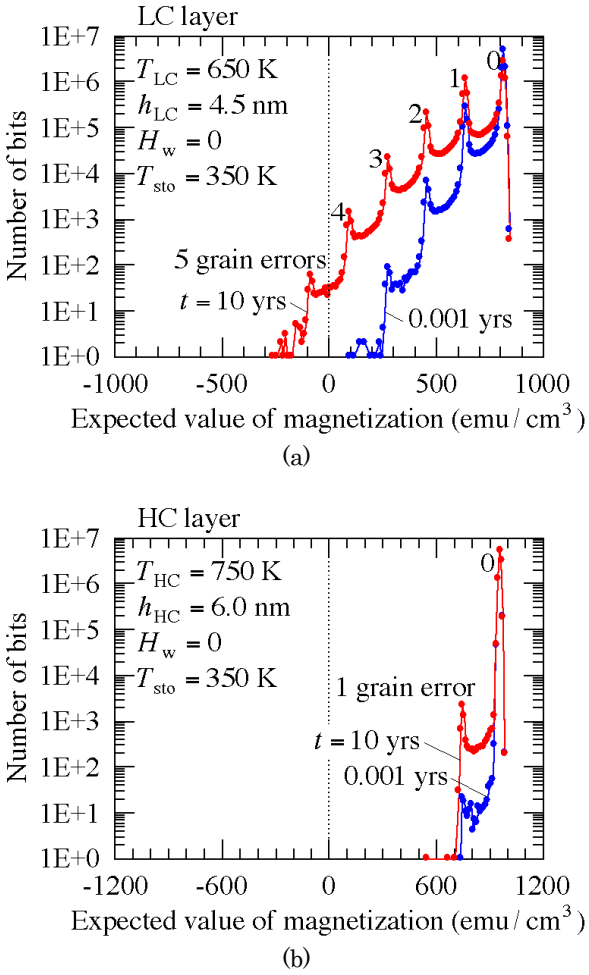

Fig. 5 Number of bits against expected value of magnetization during 10 years of archiving for the LC / HC layer structure ((a) LC and (b) HC layers).

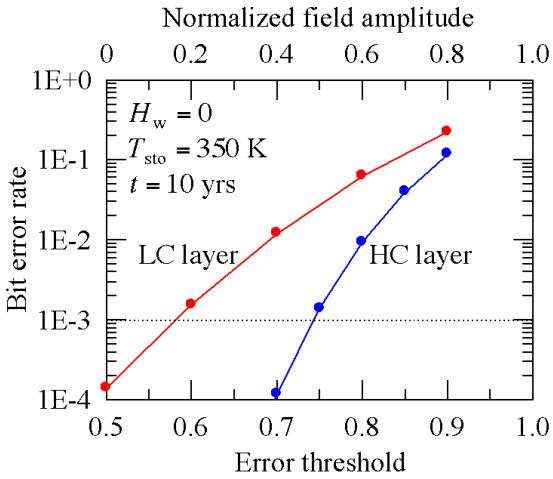

Fig. 6 Bit error rate as a function of error threshold and normalized field amplitude for 10 years of archiving for the LC / HC layer structure.

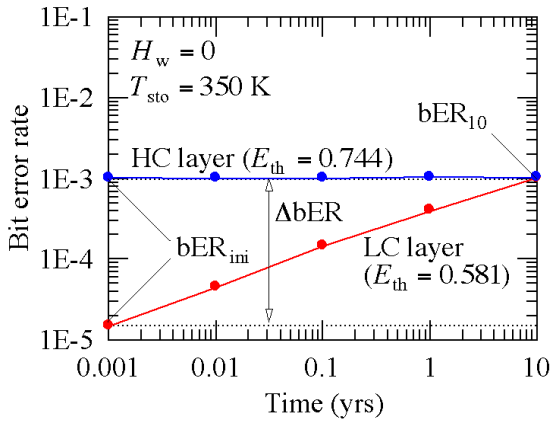

Fig. 7 Time dependence of bit error rate for 10 years of archiving for the LC / HC layer structure.

3.1.3 Information stability in HC layer while writing in LC layer

We estimated the information stability in the HC layer while writing in the LC layer using the temperature profile in **3.1.1** and the grain error probability. The writing field H_w and time t were assumed to be −10 kOe and 1 ns, respectively. Since the temperature of the 2nd row grains (track center, i = 2) is higher than that of the 1st row grains (track edge, i = 1), the number of bits against $E[M_{si}]$ averaged over one-row grains is shown in Fig. 8. The $E[M_{si}]$ value is negative for 2 or 3 grain errors since the total row grain number is three. The grain error is higher for i = 2 due to its higher temperature. For (a) T_{HC} = 750 K, only 1 grain error occurs at most in each row, and the number of errors in one bit is at most 3 in 9. On the other hand, there is 1 grain error at i = 1, and 2 grain errors at i = 2 for (b) T_{HC} = 725 K. The number of errors in one bit is at most 4 in 9. Therefore, the information in the HC layer is almost stable during writing in the LC layer.

Figure 9 shows bER as a function of E_{th} and H_0 during writing in the LC layer. When T_{HC} = 750 K, the results in Figs. 6 (HC layer) and 9 (T_{HC} = 750 K) are almost the same. Therefore, the information in the HC layer is scarcely degraded. Furthermore, there is a little degradation in the information for T_{HC} = 725 K. Since there was no change in bER over ten years in the HC layer, a bER$_{ini}$ of 1E−3 in the HC layer after writing in the LC layer can be allowable, and E_{th} values of 0.736 and 0.672 are required for T_{HC} = 750 and 725 K, respectively.

In short, the results obtained in **3.1.2** and **3.1.3** are summarized in Table 4.

Although the H_{zpeak} value is high for the LC layer as shown Fig. 3 (b), E_{th} and H_0 are low. On the other hand, E_{th} and H_0 are high in the HC layer for which H_{zpeak} is low.

The bER value in the HC layer with T_{HC} = 725 K is higher after writing in the LC layer as shown in Fig. 8. However, the HC layer with T_{HC} = 725 K as well as that with T_{HC} = 750 K may also be a candidate for 3D HAMR media with the aim of lowering T_{surf}.

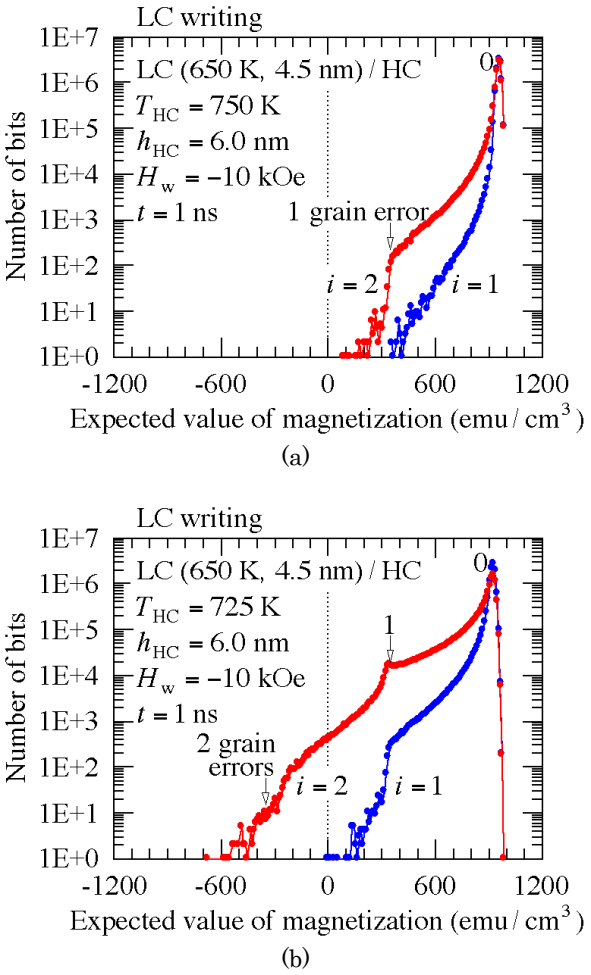

Fig. 8 Number of bits against the expected value of magnetization in the HC layer while writing in the LC layer for LC / HC layer structure ((a) T_{HC} =750 and (b) 725 K).

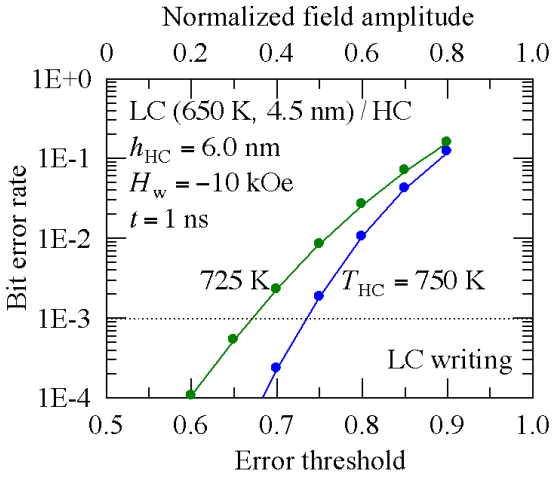

Fig. 9 Bit error rate in the HC layer as a function of the error threshold and normalized field amplitude while writing in the LC layer for LC / HC layer structure.

Table 4 Information stability results for LC / HC layer structure ((a) T_{HC} = 750 and (b) 725 K).

(a)

	LC reading	HC reading
LC / HC layer structure		
T_{cm} (K)	650	750
h (nm)	4.5	6.0
E_{th} (10 yrs of archiving)	0.581	0.744
H_0 (10 yrs of archiving)	0.16	0.49
E_{th} (LC writing)		0.736
H_0 (LC writing)		0.47
H_{zpeak} (Oe)	1151	570

(b)

	LC reading	HC reading
LC / HC layer structure		
T_{cm} (K)	650	725
h (nm)	4.5	6.0
E_{th} (10 yrs of archiving)	0.581	0.743
H_0 (10 yrs of archiving)	0.16	0.49
E_{th} (LC writing)		0.672
H_0 (LC writing)		0.34
H_{zpeak} (Oe)	1151	550

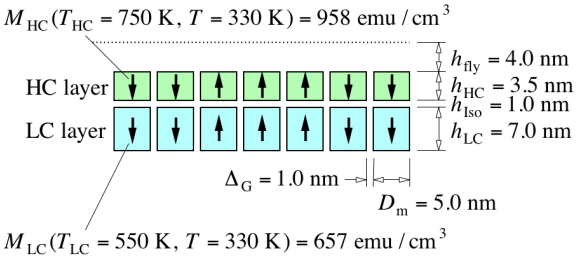

(a)

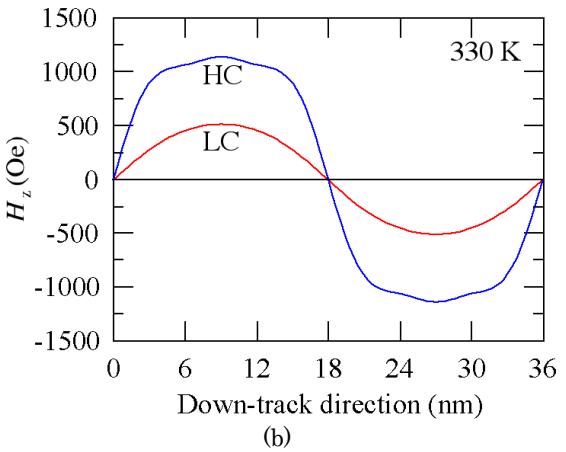

(b)

Fig. 10 (a) Layer structure for HC / LC and (b) field strength H_z from the HC and LC layers for the down-track direction.

3.2 HC / LC layer structure

Next, we discuss the structure as shown in Fig. 10 (a) where the upper layer is an HC layer with T_{HC} = 750 K and h_{HC} = 3.5 nm, and the lower layer is an LC layer with T_{LC} = 550 K and h_{LC} = 7.0 nm. The T_{LC} value must be reduced to realize information stability in the HC layer while writing in the LC layer since the ΔT_{HL} value is positive, which means that the temperature in the HC layer while writing in the LC layer is higher than that in the LC layer. Furthermore, the h_{LC} value must be increased to realize information stability in the LC layer for 10 years of archiving since T_{LC} became low.

Figure 10 (b) shows H_z at the reader from the HC and LC layers for the down-track direction. The H_{zpeak} values are 1139 and 513 Oe from the HC and LC layers, respectively, where h_{fly} is 4.0 nm.

3.2.1 Temperature profile

The results for the HC / LC layer structure are summarized in Table 5. The T_{surf} value of 874 K is relatively low since the HC layer is the upper layer. This is advantageous in terms of heat resistance.

The difference between the thermal gradients for HC and LC writing is relatively large due to the combinations of the upper HC layer and the lower LC layer. This may be disadvantageous in relation to HC and LC writing[3]. If $\partial T/\partial x$ is too large, the writing temperature decreases before writing, and write-error increases. If $\partial T/\partial x$ is too small, it is difficult to reduce the writing temperature, and the magnetization is reversed by the head field when writing the next bit. Then, erasure-after-write increases. Furthermore, if $\partial T/\partial y$ is small, the information in tracks adjacent to the writing track becomes unstable. Therefore, a small difference in the thermal gradients for HC and LC writing is preferable in terms of the writing property.

The ΔT_{HL} value of 35 K is positive. Therefore, the T_{LC} value must be reduced to realize information stability in the HC layer while writing in the LC layer, and h_{LC} must be thick to achieve information stability in the LC layer during 10 years of archiving.

Table 5 Results of heat transfer simulation for HC / LC layer structure.

	HC writing	LC writing
HC / LC layer structure		
T_{cm} (K)	750	550
h (nm)	3.5	7.0
T_{surf} (K)	874	
$\partial T / \partial x$ (K / nm)	16.6	4.9
$\partial T / \partial y$ (K / nm)	16.4	5.0
ΔT_{HL} (K)		35

3.2.2 Information stability for 10 years of archiving

Figure 11 shows the bER as a function of E_{th} and H_0 for 10 years of archiving. In comparison with the results in Fig. 6, the information stability in the HC layer has degraded since h_{HC} became thin. And although T_{LC} became low, the information stabilities in the LC layer in Figs. 6 and 11 are roughly the same since h_{LC} became thick.

The time dependence of bER is shown in Fig. 12. In comparison with Fig. 7, errors increase over time in both the HC and LC layers since h_{HC} became thin.

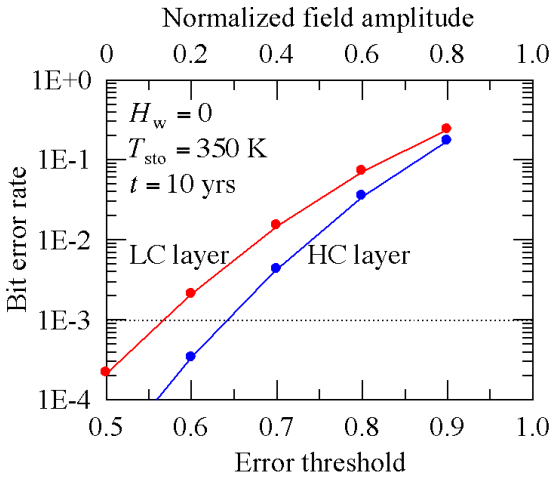

Fig. 11 Bit error rate as a function of error threshold and normalized field amplitude for 10 years of archiving for the HC / LC layer structure.

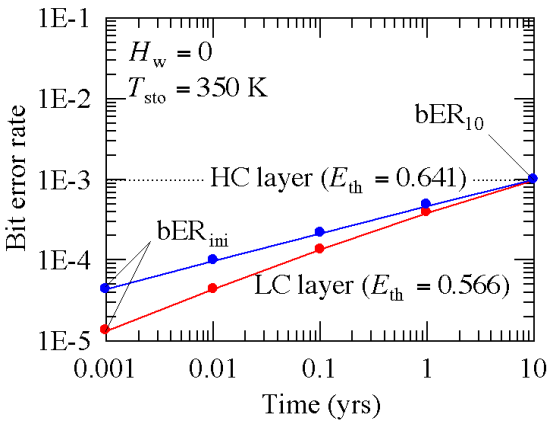

Fig. 12 Time dependence of the bit error rate for 10 years of archiving for the HC / LC layer structure.

3.2.3 Information stability in HC layer while writing in LC layer

Figure 13 shows the bER in the HC layer as a function of E_{th} and H_0 during writing in the LC layer. Since the information in the HC layer will degrade during 10 years of archiving, bER_{ini} in the HC layer after writing in the LC layer must be low, for example, 1E−4. Therefore, an E_{th} value of 0.598 is required.

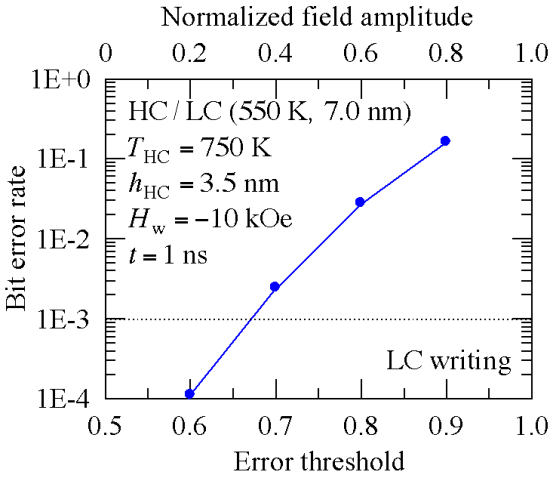

Fig. 13 Bit error rate in the HC layer as a function of error threshold and normalized field amplitude while writing in the LC layer for the HC / LC layer structure.

The results obtained in **3.2.2** and **3.2.3** are summarized in Table 6.

The H_{zpeak} value is low for the LC layer as shown Fig. 10 (b), and E_{th} and H_0 for 10 years of archiving are also low for the LC layer. Increasing the T_{LC} or h_{LC} value is necessary if we are to increase E_{th} and H_0. However, increasing the T_{LC} value leads to degradation of the information in the HC layer when writing in the LC layer since the writing temperature in the LC layer increases.

Table 6 Information stability results for HC / LC layer structure.

	HC reading	LC reading
HC / LC layer structure		
T_{cm} (K)	750	550
h (nm)	3.5	7.0
E_{th} (10 yrs of archiving)	0.641	0.566
H_0 (10 yrs of archiving)	0.28	0.13
E_{th} (LC writing)	0.598	
H_0 (LC writing)	0.20	
H_{zpeak} (Oe)	1139	513

4. Conclusions

We examined the medium layer structure in 3D HAMR at 2 Tbpsi (total density of 4 Tbpsi), taking account of a heat transfer simulation and information stability in high Curie temperature T_{HC} (HC) and low Curie temperature T_{LC} (LC) layers.

(1) An LC (T_{LC} = 650 K, 4.5 nm) / HC (T_{HC} = 750 K, 6.0 nm) layer structure

The medium surface temperature T_{surf} while writing in the HC layer is relatively high since the HC layer is the lower layer. This is disadvantageous in terms of the

heat resistance of the writing head and/or the surface lubricant.

The temperature in the HC layer while writing in the LC layer is lower than that in the LC layer, and this is advantageous in relation to the information stability in the HC layer.

Although the bit error rate in the HC layer with T_{HC} = 725 K is higher than that with T_{HC} = 750 K after writing in the LC layer, the HC layer with T_{HC} = 725 K may also be a candidate for 3D HAMR media with the aim of reducing T_{surf}.

(2) An HC (T_{HC} = 750 K, 3.5 nm) / LC (T_{LC} = 550 K, 7.0 nm) layer structure

The T_{LC} value must be reduced to realize information stability in the HC layer while writing in the LC layer.

The difference between the thermal gradients for HC and LC writing is relatively large due to the combinations of the upper HC layer and the lower LC layer. This may be disadvantageous in relation to HC and LC writing.

Acknowledgement We acknowledge the support of the Advanced Storage Research Consortium, Japan.

References

1) Western Digital: private communication.
2) T. Kobayashi, Y. Nakatani, and Y. Fujiwara: *J. Magn. Soc. Jpn.*, **44**, 34 (2020).
3) T. Kobayashi, Y. Nakatani, and Y. Fujiwara: *J. Magn. Soc. Jpn.*, **44**, 122 (2020).
4) M. Mansuripur and M. F. Ruane: *IEEE Trans. Magn.*, **MAG-22**, 33 (1986).
5) J. -U. Thiele, K. R. Coffey, M. F. Toney, J. A. Hedstrom, and A. J. Kellock: *J. Appl. Phys.*, **91**, 6595 (2002).
6) T. Kobayashi, Y. Isowaki, and Y. Fujiwara: *J. Magn. Soc. Jpn.*, **39**, 8 (2015).
7) T. Kobayashi, Y. Nakatani, and Y. Fujiwara: *J. Magn. Soc. Jpn.*, **43**, 114 (2019).
8) T. Kobayashi, Y. Nakatani, and Y. Fujiwara: *J. Magn. Soc. Jpn.*, **42**, 110 (2018).

Received Nov. 21, 2020; Accepted Dec. 17, 2020

J. Magn. Soc. Jpn., **45**, 25-29 (2021)

<Paper>

Spin Wave Resonance in Perpendicularly Magnetized Synthetic Antiferromagnets

M. Ishibashi*, Y. Shiota*, S. Funada*, T. Moriyama*, and T. Ono*, **

*Institute for Chemical Research, Kyoto University, *Uji, Kyoto 611-0011, Japan*

**Center for Spintronics Research Network, Graduate School of Engineering Science, Osaka University, *Toyonaka, Osaka 560-8531, Japan*

We report antiferromagnetic spin wave resonance in perpendicularly magnetized synthetic antiferromagnets consisting of Co/Ni multilayers and a thin Ru spacer layer. Two resonance modes were observed in the finite range of the out-of-plane bias magnetic field, where two magnetic moments separated by the Ru layer were antiferromagnetically aligned. These two modes show an opposite dependence on the bias magnetic field and correspond to right- and left-handed polarized spin waves. We also theoretically derive the spin wave dispersion for the perpendicularly magnetized synthetic antiferromagnets on the basis of an equation of motion. Our experimental results show good agreement with the theoretical analysis.

Key words: antiferromagnetic spin wave, perpendicularly magnetized synthetic antiferromagnets, polarized spin waves, spin wave resonance, multilayers

1. Introduction

Spin waves are collective excitations of ordered magnetic moments in materials and can be used as information carrier and for processing [1)-3)]. So far, most spin-wave devices have been based on ferromagnetic spin waves, and they mainly use spin wave amplitude [4)-7)] and phase [8)-10)] to encode information. Unlike ferromagnetic spin waves, spin waves in colinear antiferromagnets have both right- and left-handed polarizations [11)-12)], as shown in Fig. 1. The polarity of antiferromagnetic spin waves is attracting much attention in the recent research field of magnonics, as a new degree of freedom [13)-14)], in addition to the amplitude and phase. In the past several decades, magnetic resonances with the two kinds of polarities were observed in uniaxial crystal antiferromagnets such as MnF_2 [15)] or FeF_2 [16)]. However, it is difficult to excite or manipulate spin waves in crystal antiferromagnets, because they have high resonance frequency of THz regime due to strong exchange coupling. Recent works have focused on not only crystal antiferromagnets but also ferrimagnets for spin wave polarization experiments. In the previous studies, right- and left-handed spin wave polarizations were directly observed by inelastic neutron scattering in yttrium iron garnet [17)] and switching of spin wave polarization was observed across the compensated temperature by Brillouin light scattering in GdFeCo films [18)].

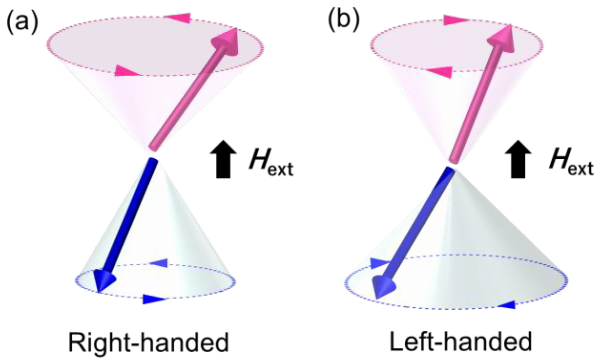

Fig. 1 Schematic illustrations of magnetic oscillations of two antiparallel sublattices for (a) right- and (b) left-handed polarity.

In synthetic antiferromagnets (SAFs), two magnetic moments separated by a thin nonmagnetic spacer are antiferromagnetically coupled via interlayer exchange coupling. SAFs show weaker exchange interaction than that in crystal antiferromagnets, hence, resonance frequencies of SAFs are in the range of conventional microwave electronics (several tens of GHz regime). These features of SAFs can allow easier detection and manipulation of the antiferromagnetic spin wave modes. In this study, we experimentally investigate spin wave resonance in perpendicularly magnetized SAFs by spectroscopy using a vector network analyzer.

2. Theoretical Analysis

We begin with a theoretical calculation of spin wave dispersion for interlayer exchange coupled bilayers with perpendicular magnetic anisotropy (PMA). We consider the system including two ferromagnetic layers FM1, FM2 with the same thickness t, the same saturation magnetization M_s, and different magnetic anisotropy $K_1 \neq K_2$. Spin wave dispersion with wavevector k can be derived from an equation of motion (EOM) including the dynamic dipolar field due to the nonuniform distribution of local magnetic moments of spin waves. The effective field $\mathbf{H}_i$ ($i = 1, 2$) acting on the magnetization $\mathbf{m}_i$ ($|\mathbf{m}_i| = 1$) of the FM i layer is given by

$$\mathbf{H}_i = \left\{H_{\text{ext}} + \left(\frac{2K_i}{\mu_0 M_s} - M_s\right) m_{Zi}\right\} \mathbf{e}_Z - H_E \mathbf{m}_j + \mathbf{H}_{\text{dip},ii} + \mathbf{H}_{\text{dip},ij}, \quad (i, j = 1, 2, i \neq j) \quad (1)$$

where H_E represents the exchange field. The precession of a magnetic moment in the FM i layer can be expressed by normalized magnetization $\mathbf{m}_i = (m_{Xi}, m_{Yi}, m_{Zi})$. The Z axis is parallel to the direction of the out-of-plane magnetic field H_{ext} and X axis is parallel to spin wave propagation direction. The last two terms correspond to the self- and mutual-dipolar fields (given in the Appendix A) [19)-23)].

The EOM, $d\mathbf{m}_i/dt = -\mu_0\gamma\mathbf{m}_i \times \mathbf{H}_i$, can be linearized by assuming small deviation of the magnetization from the static magnetization direction, $|m_{Xi}|, |m_{Yi}| \ll 1$, and the linearized EOM is given by

$$i\omega \begin{pmatrix} m_{X_1} \\ m_{Y_1} \\ m_{X_2} \\ m_{Y_2} \end{pmatrix} + \mu_0\gamma\hat{\mathbf{H}} \begin{pmatrix} m_{X_1} \\ m_{Y_1} \\ m_{X_2} \\ m_{Y_2} \end{pmatrix} = 0\,, \qquad (2)$$

where γ is the gyromagnetic ratio. The resonance frequencies $f = \omega/(2\pi)$ are obtained as the eigenvalues of the 4th order matrix $\hat{\mathbf{H}}$, whose elements are explicitly given in the Appendix B.

In the case of antiparallel state, $m_{Z1} \simeq 1$ and $m_{Z2} \simeq -1$ (as shown in the inset of Fig.4), the two resonance frequencies are given by

$$f_1 = \frac{\mu_0\gamma}{2\pi}\sqrt{H_a - \sqrt{H_b}}\,, \qquad (3)$$

$$f_2 = \frac{\mu_0\gamma}{2\pi}\sqrt{H_a + \sqrt{H_b}}\,, \qquad (4)$$

$$H_a = {H_{\rm ext}}^2 + H_{\rm ext}H_B + H_E H_A + \frac{{H_{k1}}^2 + {H_{k2}}^2}{2} + \frac{H_A k M_s t}{4}\,,$$

$$H_b = H_A\left\{\left(H_{\rm ext} + \frac{H_B}{2}\right)^2 (4H_E + H_A) + \left(H_{\rm ext} + \frac{H_B}{2}\right)^2 k M_s t + \frac{H_A k^2 M_s^2 t^2}{16}\right\},$$

where $H_A = H_{k1} + H_{k2}$, $H_B = H_{k1} - H_{k2}$ and the effective magnetic anisotropy field $H_{ki} = 2K_i/(\mu_0 M_s) - M_s$. For spin waves with $k = 0\ \mu\text{m}^{-1}$, the resonance frequencies become simpler forms as below

$$f_\pm = \frac{\mu_0\gamma}{4\pi}\{\pm(2H_{\rm ext} + H_{k1} - H_{k2}) + \sqrt{(H_{k1} + H_{k2})(4H_E + H_{k1} + H_{k2})}\}. \qquad (5)$$

f_+ (f_-) increases (decreases) linearly with the applied out-of-plane magnetic field. Here, f_+ (f_-) is the resonance frequency for right (left)-handed polarization [24)-25)] shown in Fig. 1.

3. Magnetic Properties for Sample Films

Films of Ta(3.0) / Pt(2.0) / [Co(0.2) / Ni(0.7)]$_5$ / Co(0.2) / Ru(0.5) / [Co(0.2) / Ni(0.7)]$_5$ / Co(0.2) / Ru(3.0) (unit: nm) were deposited using dc magnetron sputtering on thermally oxidized Si substrates. Two ferromagnetic layers consisting of Co/Ni multilayers are separated by a 0.5 nm-thick Ru layer. Figure 2 shows out-of-plane magnetic hysteresis loop obtained by using superconducting quantum interference device magnetometer. Magnetic moments in the two ferromagnetic layers are perpendicular to the film plane and fully compensated under the out-of-plane magnetic field from 160 mT to −190 mT (from −160 mT to 190 mT). From this result, we determined the saturation magnetization $M_s = 7.0 \times 10^5$ A/m and the exchange field $\mu_0 H_E = J/M_s t = 180$ mT, where the symbol of J represents the interlayer exchange coupling [26)].

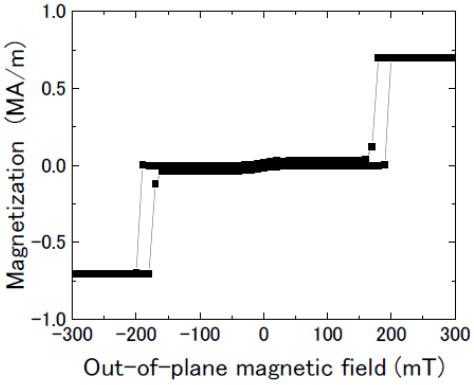

Fig. 2 Magnetic hysteresis loop measured at 300 K under out-of-plane magnetic field.

4. Experimental Procedure and Results

The films were patterned into 50 × 100 μm^2 rectangular wires and then 80 nm-thick SiO_2 was deposited for electrical isolation. Subsequently, we fabricated coplanar waveguides for spin wave resonance (SWR) as shown in Fig. 3 (a). Coplanar wave guides were designed for excitation of spin waves with $k = 1.2\ \mu\text{m}^{-1}$. Re [$S_{11}$] spectra were obtained by spectroscopy using a vector network analyzer at a given out-of-plane magnetic field. Figure 3 (b) shows a contour plot of SWR spectra generated from the obtained Re [S_{11}] spectra. The applied magnetic field swept from 250 mT to –250 mT with a step of 10 mT. Two resonance modes were observed from 130 mT to –190 mT, where the two magnetic moments were antiferromagnetically aligned. The slight difference of the field range for the antiparallel state between SQUID and SWR measurements can be due to undesirable changes in the properties of the films during the patterning process. The observed two modes cross at –100 mT and are split by the out-of-plane magnetic field.

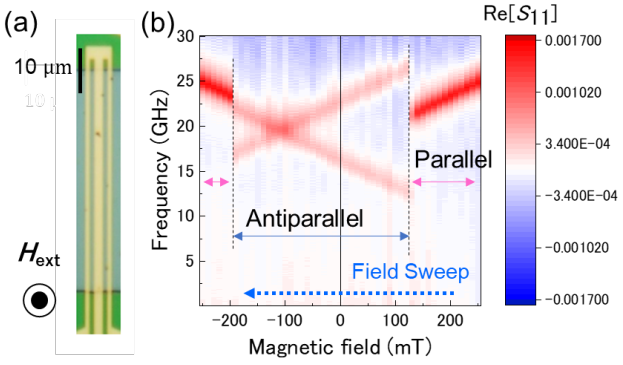

Fig.3 (a) Optical micrograph of device for investigating of SWR spectra. Bias magnetic field was applied out of-plane. (b) Contour plot of Re [S_{11}].

5. Discussion

In our experimental case, the attenuation length is estimated to be less than 50 nm from the calculation of $L = v_g/(2\pi f\alpha)$ where L represents the attenuation length, $v_g = \partial(2\pi f)/\partial k$ represents the group velocity, f represents the resonance frequency expressed by Eqs. (3) (4) and $\alpha = 0.024$ represents the damping constant for Co/Ni multilayers [27]. Our coplanar waveguides shown in Fig.3 (a) have a distance of 1 μm between signal and ground antennas. These conditions imply that excited spin waves under one antenna decay before they reach the other two antennas, and that spin waves under each antenna can be regard as localized uniform precession mode. Therefore, we analyzed our experimental data with the resonance frequencies for spin waves with $k = 0$ μm^{-1}. We can obtain the average of PMA for two ferromagnetic layers $(K_1 + K_2)/2$, by linear fitting of the experimental data above 140 mT and below –200 mT with Eq.(17) for parallel state (the details are in the Appendix C). On the other hand, we can obtain the difference of PMA $(K_2 - K_1)/2$ by linear fitting of the experimental data from –190 to 130 mT with Eq. (5) for antiparallel state, because the intersection magnetic field of the two antiferromagnetic resonance modes is given by $(H_{k2} - H_{k1})/2$ which represents the difference of the effective magnetic field between the two ferromagnetic layers as predicted in a previous report [28]. While our films consist of two ferromagnetic layers with the same structure, the experimental results shown in Fig. 3 (b) suggests that they have different PMA, indicating the Pt under layer induces the stronger PMA in the adjacent (lower) ferromagnetic layer.

Figure 4 shows the applied magnetic field dependence of the resonance frequencies obtained from the theoretical spin wave dispersion for $k = 0$ μm^{-1} (Black lines represent parallel state case, while red and blue lines represent antiparallel state case.) with experimentally determined parameters ($\gamma = 1.88 \times 10^{11}$ rad/Ts, $M_S = 7.0 \times 10^5$ A/m ,t =4.7 nm, $J = 5.9 \times 10^{-4}$ J/m^2, $K_1 = 5.4 \times 10^5$ J/m^3, $K_2 = 4.7 \times 10^5$ J/m^3), which gives a good agreement with our experimental data shown in Fig. 3 (b). For the case of parallel state, two resonance frequencies f_{P_In} and f_{P_Out} are theoretically derived (Eqs. (17) (18) in the Appendix C), corresponding to in-phase and out-of-phase precession modes. It should be noted that it is difficult to observe the magnetic resonance for the out-of-phase precession mode, because two ferromagnetic layers are almost identical. For the case of antiparallel state, with comparison of the experimental results and the theoretical analysis, our observed two resonance modes showing opposite tendencies with the bias magnetic field can be presumed to be $f_\pm$ in Eq. (5), corresponding to right- and left-handed polarized spin waves. These two oppositely polarized modes are degenerated at the cross point.

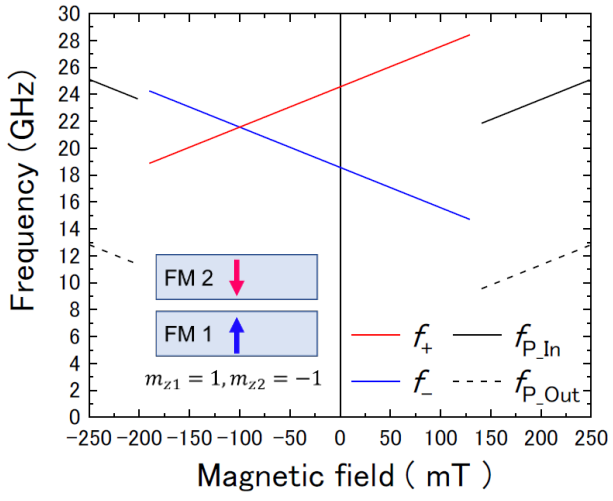

Fig.4 Applied magnetic field dependence of resonance frequencies calculated by theoretical spin wave dispersion with $k = 0$ μm^{-1} [f_+ and f_- are for case of antiparallel state Eq. (5)]. f_{P_In} and f_{P_Out} are for case of parallel state [Eqs. (17) (18) in Appendix C].

6. Conclusion

In summary, we experimentally and theoretically demonstrated spin wave resonance in perpendicularly magnetized SAFs. In the finite range of the applied out-of-plane magnetic field, two resonance modes for antiferromagnetic state were observed, and they correspond to right- and left-handed polarized spin waves. Our findings will give a route to spin-wave-devices utilizing spin wave polarization, based on SAFs.

Acknowledgements This work was partially supported by the JSPS KAKENHI Grant Numbers JP15H05702, JP18K19021, JP20H00332, JP20K15161, JP20J15421, and by the Collaborative Research Program of the Institute for Chemical Research, Kyoto University, and by the Cooperative Research Project Program of the Research Institute of Electrical Communication, Tohoku University.

Appendix

A. Self-dipolar field and mutual dipolar field

For interlayer exchange coupled bilayers with PMA, magnetostatic energy per unit area is given by

$$E = -\sum_{i=1,2} \mu_0 M_S t_i \mathbf{m}_i \cdot \mathbf{H}_{ext} - \sum_{i=1,2} (K_i t_i - \frac{\mu_0}{2} M_S{}^2) m_{Zi}{}^2 + J\mathbf{m}_1 \cdot \mathbf{m}_2, \quad (6)$$

where $\mathbf{H}_{ext} = (0, 0, H_{ext})$, Z axis is perpendicular to the film plane, X axis is parallel to the spin wave propagation direction, the first term is Zeeman energy, the second term is demagnetization, the third term is PMA energy and the last term is interlayer exchange energy.

The effective field is given by

$$\mathbf{H}_i = -\nabla_{\mathbf{m}_i}\left(\frac{E}{\mu_0 M_S t}\right) + \mathbf{H}_{\mathrm{dip},ii} + \mathbf{H}_{\mathrm{dip},ij},\ \ (i,j=1,2,i\neq j) \quad (7)$$

where $\mathbf{H}_{\mathrm{dip},ii}$ represents the self-dipolar fields and $\mathbf{H}_{\mathrm{dip},ij}$ represents the mutual-dipolar field.

$\mathbf{H}_{\mathrm{dip},ii}$ and $\mathbf{H}_{\mathrm{dip},ij}$ can be obtained by using the Green function [21)-23)], given by

$$G_{XYZ}(Z-Z') = \begin{pmatrix} -G_P & 0 & iG_Q \\ 0 & 0 & 0 \\ iG_Q & 0 & G_P - \delta(Z-Z') \end{pmatrix}, \quad (8)$$

where $G_P = (k/2)\exp(-k|Z-Z'|)$ and $G_Q = G_P \mathrm{sgn}(Z-Z')$. The self-dipolar fields $\mathbf{H}_{\mathrm{dip},ii}$ can be calculated by

$$\mathbf{H}_{\mathrm{dip},ii} = \frac{M_s}{t}\int_{s/2}^{t+s/2} dZ \int_{s/2}^{t+s/2} dZ'\, G_{XYZ}(Z - Z')\delta\mathbf{m}(Z-Z'). \quad (9)$$

The mutual-dipolar field $\mathbf{H}_{\mathrm{dip},ij}$ can be calculated by

$$\mathbf{H}_{\mathrm{dip},21} = \frac{M_s}{t}\int_{s/2}^{t+s/2} dZ \int_{-t-s/2}^{-s/2} dZ'\, G_{XYZ}(Z-Z')\delta\mathbf{m}(Z-Z'), \quad (10)$$

$$\mathbf{H}_{\mathrm{dip},12} = \frac{M_s}{t}\int_{-t-s/2}^{-s/2} dZ \int_{s/2}^{t+s/2} dZ'\, G_{XYZ}(Z-Z')\delta\mathbf{m}(Z-Z'), \quad (11)$$

where $\delta\mathbf{m}(Z-Z')$ represents relative perturbation oscillation of a magnetic moment at Z' position against a magnetic moment at Z position

$$\delta\mathbf{m}(Z-Z') = e^{-k|Z-Z'|}\begin{pmatrix} m_X(Z') \\ m_Y(Z') \\ 0 \end{pmatrix}, \quad (12)$$

and s represents the thickness of a nonmagnetic spacer between two ferromagnetic films.

By assuming $ks, kt \ll 1$, we can obtain $\mathbf{H}_{\mathrm{dip},ii}$ given by

$$\mathbf{H}_{\mathrm{dip},ii} = M_S t\begin{pmatrix} -\frac{k}{2}m_{Xi} \\ 0 \\ 0 \end{pmatrix}, \quad (13)$$

and we can obtain $\mathbf{H}_{\mathrm{dip},12}$ and $\mathbf{H}_{\mathrm{dip},21}$ given by

$$\mathbf{H}_{\mathrm{dip},12} = M_S t\begin{pmatrix} -\frac{k}{2}m_{X2} \\ 0 \\ -i\frac{k}{2}m_{X2} \end{pmatrix}, \quad (14)$$

$$\mathbf{H}_{\mathrm{dip},21} = M_S t\begin{pmatrix} -\frac{k}{2}m_{X1} \\ 0 \\ i\frac{k}{2}m_{X1} \end{pmatrix}. \quad (15)$$

B. Resonant frequency for antiparallel state

The spin wave resonant frequency is obtained from the EOM, $\mathrm{d}\mathbf{m}_i/\mathrm{d}t = -\mu_0\gamma\mathbf{m}_i \times \mathbf{H}_i$, linearized by assuming $|m_{Xi}|, |m_{Yi}| \ll 1$. In the case of antiparallel state, $m_{Z1} \simeq \pm 1$ and $m_{Z2} \simeq \mp 1$, the linearized EOM is explicitly given by

$$\mathrm{i}\omega\begin{pmatrix} m_{X_1} \\ m_{Y_1} \\ m_{X_2} \\ m_{Y_2} \end{pmatrix} + \mu_0\gamma\begin{pmatrix} 0 & H_{12} & 0 & H_{14} \\ H_{21} & 0 & H_{23} & 0 \\ 0 & H_{32} & 0 & H_{34} \\ H_{41} & 0 & H_{43} & 0 \end{pmatrix}\begin{pmatrix} m_{X_1} \\ m_{Y_1} \\ m_{X_2} \\ m_{Y_2} \end{pmatrix} = 0. \quad (16)$$

Here, the components of 4th order matrix of the effective field $\hat{\mathbf{H}}$ are given by

$$H_{12} = H_{\mathrm{ext}} \pm H_{k1} \pm H_{\mathrm{E}},$$
$$H_{14} = \pm H_{\mathrm{E}},$$
$$H_{21} = -(H_{\mathrm{ext}} \pm H_{k1} \pm H_{\mathrm{E}}) \mp (kMt)/2,$$
$$H_{23} = \mp H_{\mathrm{E}} \mp (kMt)/2,$$
$$H_{32} = \mp H_{\mathrm{E}},$$
$$H_{34} = H_{\mathrm{ext}} \mp H_{k2} \mp H_{\mathrm{E}},$$
$$H_{41} = \pm H_{\mathrm{E}} \pm (kMt)/2,$$
$$H_{43} = -(H_{\mathrm{ext}} \mp H_{k2} \mp H_{\mathrm{E}}) \pm (kMt)/2,$$

the resonant frequency $f = \omega/2\pi$ is eigenvalue of the matrix $\hat{\mathbf{H}}$: $\det[i\omega\hat{\mathbf{1}} + \mu_0\gamma\hat{\mathbf{H}}] = 0$, where $\hat{\mathbf{1}}$ is the 4th order identity matrix. The obtained two resonance frequencies for antiparallel state are already presented in the main text as Eqs. (3) (4).

C. Resonant frequency for parallel state

In the case of parallel state, $m_{z1} \simeq \pm 1$ and $m_{z2} \simeq \pm 1$, the components of 4th order matrix of the effective field $\hat{\mathbf{H}}$ in Eq. (16) are given by

$$H_{12} = H_{\mathrm{ext}} \pm H_{k1} \mp H_{\mathrm{E}},$$
$$H_{14} = \pm H_{\mathrm{E}},$$
$$H_{21} = -(H_{\mathrm{ext}} \pm H_{k1} \mp H_{\mathrm{E}}) \mp (kMt)/2,$$
$$H_{23} = \mp H_{\mathrm{E}} \mp (kMt)/2,$$
$$H_{32} = \pm H_{\mathrm{E}},$$
$$H_{34} = H_{\mathrm{ext}} \pm H_{k2} \mp H_{\mathrm{E}},$$
$$H_{41} = \mp H_{\mathrm{E}} \mp (kMt)/2,$$
$$H_{43} = -(H_{\mathrm{ext}} \pm H_{k2} \mp H_{\mathrm{E}}) \mp (kMt)/2.$$

As well as the antiparallel state case, two resonance frequencies can be obtained from the eigenvalues of the Eq. (16) for parallel state case. For $k = 0$ μm^{-1}, the in-phase and out-of-phase resonance frequencies $f_{\mathrm{P\_In}}$ and $f_{\mathrm{P\_Out}}$ for the case of $m_{Z1} \simeq 1$ and $m_{Z2} \simeq 1$, (or $m_{Z1} \simeq -1$ and $m_{Z2} \simeq -1$) are given by

$$f_{\mathrm{P\_In}} = \frac{\mu_0\gamma}{4\pi}\left\{2|H_{\mathrm{ext}}| - 2H_{\mathrm{E}} + H_{k1} + H_{k2} + \sqrt{4{H_{\mathrm{E}}}^2 + (H_{k1}-H_{k2})^2}\right\}. \quad (17)$$

$$f_{\mathrm{P\_Out}} = \frac{\mu_0\gamma}{4\pi}\left\{2|H_{\mathrm{ext}}| - 2H_{\mathrm{E}} + H_{k1} + H_{k2} - \sqrt{4{H_{\mathrm{E}}}^2 + (H_{k1}-H_{k2})^2}\right\}. \quad (18)$$

The intercept of Eq. (17) is expressed by H_{E}, $(H_{k1}+H_{k2})$ and $(H_{k1}-H_{k2})$. The difference of effective magnetic anisotropy field between two ferromagnetic layers $(H_{k1}-H_{k2})$ can be obtained by the intersection magnetic field of two antiferromagnetic resonance modes expressed by Eq. (5). Therefore, we can obtain the sum of effective magnetic anisotropy field $(H_{k1}+H_{k2})$.

References

1) V. V. Kruglyak, S. O. Demokritov, and D. Grundler, *J. Phys. D. Appl. Phys.* **43**, 264001 (2010).
2) A. A. Serga, A. V. Chumak and B. Hillebrands, *J. Phys. D: Appl. Phys.* **43**, 264002 (2010).
3) A. V. Chumak, V. I. Vasyuchka, A. A. Serga, and B. Hillebrands, *Nat. Phys.* **11**, 453 (2015).
4) A. V. Chumak, A. A. Serga, and B. Hillebrands, *Nat. Commun.* **5**, 4700 (2014).
5) K. Vogt, F.Y. Fradin, J.E. Pearson, T. Sebastian, S.D. Bader, B. Hillebrands, A. Hoffmann and H. Schultheiss, *Nat. Commun.* **5**, 3727 (2014).
6) F. Garcia-Sanchez, P. Borys, R. Soucaille, J.-P. Adam, R. L. Stamps, and Joo-Von Kim, *Phys. Rev. Lett.* **114**, 247206 (2015).

7) K. Wagner, A. Kákay, K. Schultheiss, A. Henschke, T. Sebastian, and H. Schultheiss, *Nat. Nanotechnol.* **11**, 432 (2016).
8) R. Hertel, W. Wulfhekel, and J. Kirschner, *Phys. Rev. Lett.* **93**, 257202 (2004).
9) K. S. Lee and S. K. Kim, *J. Appl. Phys.* **104**, 053909 (2008).
10) S. Klingler, P. Pirro, T. Brächer, B. Leven, B. Hillebrands, and A. V. Chumak, *Appl. Phys. Lett.* **105**, 152410 (2014).
11) F. Keffer and C. Kittel, *Phys. Rev.* **85**, 329 (1952).
12) F. Keffer, H. Kaplan, and Y. Yafet, *Am. J. Phys.* **21**, 250 (1953).
13) R. Cheng, M. W. Daniels, J. G. Zhu, and D. Xiao, *Sci. Rep.* **6**, 24223 (2016).
14) J. Lan, W. Yu, and J. Xiao, *Nat. Commun.* **8**, 178 (2017).
15) M. Hagiwara, K. Katsumata, H. Yamamaguchi, M. Tokunaga, I. Yamada, M. Gross, and P. Goy, *Int. J. Infrared Millimeter Waves*. **20**, 617 (1999).
16) M. T. Hutchings, B. D. Rainford, and H. J. Guggenheim, *J. Phys. C Solid State Phys.* **3**, 307 (1970).
17) Y. Nambu, J. Barker, Y. Okino, T. Kikkawa, Y. Shiomi, M. Enderle, T. Weber, B. Winn, M. Graves-Brook, J. M. Tranquada, T. Ziman, M. Fujita, G. E. W. Bauer, E. Saitoh, and K. Kakurai, *Phys. Rev. Lett.* **125**, 27201 (2020).
18) C. Kim, S. Lee, H. Kim, J. Park, K. Moon, J. Y. Park, J. M. Yuk, K. Lee, B. Park, S. K. Kim, K. Kim, and C. Hwang, *Nat. Mater.* **19**, 980 (2020).
19) B. A. Kalinikos and A. N. Slavin, *J. Phys. C Solid State Phys.* **19**, 7013 (1986).
20) R. L. Stmps, *Phys. Rev. B* **49**, 339 (1994).
21) H. Skarsvåg, A. Kapelrud, and A. Brataas, *Phys. Rev. B* **90**, 094418 (2014).
22) M. Ishibashi, Y. Shiota, T. Li, S. Funada, T. Moriyama, T. Ono, *Sci. Adv.* **6**, eaaz6931 (2020).
23) Y. Shiota, T. Taniguchi, M. Ishibashi, T. Moriyama, and T. Ono, *Phys. Rev. Lett.* **125**, 017203 (2020).
24) A. G. and G. Melkov, *Magnetization Oscillations and Waves* (CRC Press, Cleveland, 1996).
25) S. M. Rezende, *Fundamentals of Magnonics* (Springer, Cham, 2020).
26) H. Bloemen, M. Swagten, and M. De Jonge, *Phys. Rev. B* **50**, 13505 (1994).
27) J. Han, P. Zhang, J. T. Hou, S. A. Siddiqui, L. Liu, *Science* **366**, 1121-1125 (2019).
28) T. Devolder, *J. Appl. Phys.* **119**, 153905 (2016).

Received Nov. 04, 2020; Accepted Jan. 05, 2021

J. Magn. Soc. Jpn., **45**, 30-36 (2021)

<Paper>

Void-Defect Induced Magnetism and Structure Change of Carbon Materials - I : Graphene Nano Ribbon

Norio Ota and Laszlo Nemes*

Graduate School of Pure and Applied Sciences, University of Tsukuba, *1-1-1 Tenoudai Tsukuba-city 305-8571, Japan*,

*Research Center for Natural Sciences, Ötvös Lóránd Research Network, *Budapest 1519, Hungary*

Void-defect is a possible origin of ferromagnetic-like feature of pure carbon material. Applying density functional theory to void-defect induced graphene-nano-ribbon (GNR), a detailed relationship between multiple-spin-state and structure change was studied. An equilateral triangle of an initial void having six electrons is distorted to isosceles triangle by re-bonding carbon atoms. Among possible spin-states of S_z=0/2, 2/2, 4/2 and 6/2, the most stable state was S_z=2/2. The case of S_z=4/2 is remarkable that initial flat ribbon turned to three dimensionally curled one having highly polarized spin configuration at ribbon edges. Total energy of S_z=4/2 was very close to that of S_z=2/2, which suggests coexistence of flat ribbon and curled ribbon. As a model of three dimensional graphite, bi-layered AB stacked GNR was analyzed for cases of different void position of α-site and ß-site. Spin distribution was limited to the surface layer, nothing to the back layer. Distorted void triangle show 60degree clockwise rotation from α- to ß-site, which was consistent with experimental observation using the scanning tunneling microscope. This study revealed that void-defect in GNR induces unusual polarized spin state, different with usual ferromagnetic one.

Key words: graphene, GNR, DFT, void, ferromagnetism, spin state, STM

1. Introduction

These ten years, it was reported that some carbon base materials show room temperature ferromagnetic like hysteresis[1)-6)]. They are graphite and graphene like materials. Such a light-weight ferromagnetic like materials will be useful for many applications. However, such magnetic ordering could not be thoroughly understood. Possible explanations are the presence of impurities[7)], edge irregularities[8)-10)] or void-defects[11)-16)]. Here, we like to focus on void-defect. In experiments, creation of void-defect was done by high energy particle irradiation on graphite[11)-13)]. Void-defect was observed by the scanning tunneling microscope[14)-16)]. Unfortunately, there are little information on magnetic behaviors and spin distributions in atomic scale. Theoretical calculations predicted the importance of the atomic structure change[17)-18)]. However, there are little explanation on a detailed relationship between the multiple-spin-state and the structure-change. Here, we try detailed explanation by the density functional theory (DFT) [19-20)]. DFT gives the stable quantum state basically at zero temperature. In this study, we like focus on fundamental property of void-defect induced magnetism and structure change of graphene nano ribbon (GNR). Such analysis will be useful for future advanced study on room temperature magnetism and asking Curie-temperature.

There are six unpaired electrons around one void, which suggests a capability of multiple spin-state as like S_z=6/2, 4/2, 2/2, and 0/2. We need detailed spin dependent calculation to find the most stable spin state accompanying with the structure change Also, we will calculate the three-dimensional graphite using the model of AB-stacked bi-layer GNR. Results will be compared with experimental observation by the scanning tunneling microscope.

2. Calculation Method and Model GNR

We require total energy, optimized molecular structure and the spin density on a given spin state of S_z. DFT based generalized gradient approximation (GGA-PBEPBE) [21)] was applied utilizing Gaussian09 package[22)] with an atomic orbital 6-31Gd basis set[23)]. Total charge is set to be completely zero. Inside of a super-cell, three dimensional DFT was applied. As illustrated in Fig. 1, one dimensional periodic boundary condition was applied to realize an unlimited length GNR. Calculation is repeated until to meet the convergence criteria on the root mean square density matrix less than 10^{-8} within 128 cycles.

An initial calculation model of GNR with single void-defect is shown in left of Fig. 1. Super-cell was [$C_{79}H_{10}$], where upper and lower zigzag edge carbons were all hydrogenated to avoid radical carbon edge complicated situation. Ribbon width was 1.780nm and one-dimensional super-cell length was 1.241nm repeating to red-line direction. A center positioned carbon was removed to make a void-defect. Around this void, there are three carbons, which make an equilateral triangle with length of 0.248nm. These three radical carbons bring six electrons. To investigate magnetic characteristics, we should consider these six electrons interaction, which mean to study a detailed multiple-spin-state analysis.

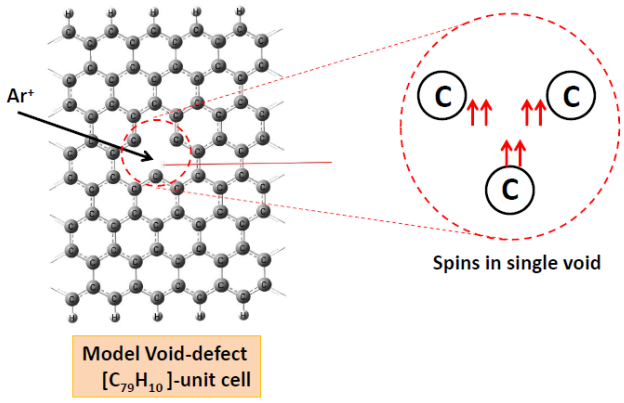

Fig. 1 Initial void-defect is created on GNR. Six spins in a void carry the multiple spin state. Unit cell is $[C_{79}H_{10}]$. DFT calculation is done three dimensionally inside of unit cell, which is repeated one dimensionally toward a red line direction.

.

3. Multiple Spin State

For six electrons in a void-defect, there are four capable spin states of S_z=0/2, 2/2, 4/2 and 6/2. However, we could not get any converged calculation on singlet spin state of S_z=0/2. The reason will be explained as illustrated on right of Fig. 1 that one radical carbon holds two spins, which should be parallel to avoid unlimited large coulomb energy due to Hund's rule[24], in case of one central attractive force by the same carbon atom. Three pairs of parallel spins enable the multiple-spin-state of S_z=6/2, 4/2, or 2/2. For every spin state, stable atomic structures are classified to two types as Type-A and -B as shown in Fig. 2 as (b) and (c). It should be noted that initial equilateral triangle (a) turned to an isosceles one of (b) and (c). Isosceles triangle of Type-A was perpendicular to a ribbon axis of a red line, whereas Type-B tilted. Such distortion originates from the quantum mechanical re-bonding as discussed by Yazyev and Helm[17]. Detailed results were shown in Fig. 3 and Table 1. Initial non-deformed ribbon energy was defined to be zero. In Type-A, the most stable spin state was S_z=2/2. Energy level was reduced to -12.31kcal/mol., where triangle has an angle of 49degree as shown in (b). Type-B show remarkable energy reduction. In case of S_z=2/2 of Type-B, energy became -15.62kcal/mol, which is most stable one with a sharper angle of 44degree in (c). Distance between carbon-atom "a" and "c" was shortened to 0.192nm from original 0.248nm. This suggests a capable origin of structure change that original pi-electron conjugated bond is partially modified to double-bond among hexagon carbon networks.

Sum of spin density around initial equilateral void was 1.49μB, which coincides well with calculation using the SIESTA code by Yazyev and Helm[17]. Spin densities of Type-A (S_z=2/2) and B (S_z=2/2) were illustrated in Fig. 4 at a surface of electron density of 1e/nm^3. In both cases, we can see a large up-spin cloud (red) at a void triangle's apex carbon site. We can see fruit pear like up-spin cloud with sum of 1.37μB, which was 0.12μB smaller than initial one. Inside of GNR, there appears up (red) and down (blue) spins alternatively[9-10].

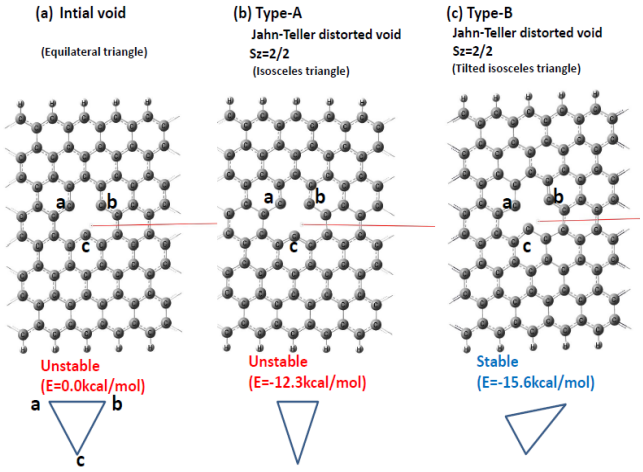

Fig. 2 Initial void makes equilateral triangle. Type-A has an isosceles triangle perpendicular to GNR, whereas Type-B tilted.

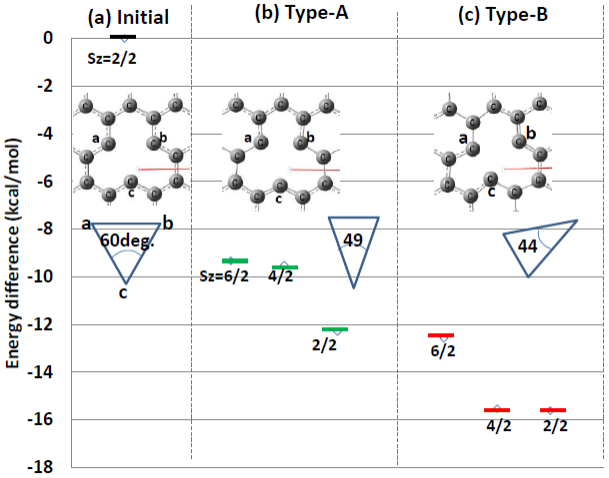

Fig. 3 Energy difference and void structure change. Type-A show distorted isosceles void triangle of 49degree perpendicular to ribbon as shown in (b). Type-B shows a tilted triangle with 44degree. In every type, triplet spin-state of S_z=2/2 is most stable.

Table 1 Calculated result for mono layer GNR.

Distorted type	none	Type A			Type B		
Case number	A0	A1	A2	A3	B1	B2	B3
Given Sz	2/2	6/2	4/2	2/2	6/2	4/2	2/2
Energy difference (kcal/mol/unit cell)	0	−9.33	−9.51	−12.31	−12.58	−15.54	−15.62
Ribbon configuration	Flat	Flat	Flat	Flat	Flat	Curled	Flat
Triangle distance ab	2.48	2.15	2.11	2.14	2.59	2.61	2.59
(A) bc	2.48	2.6	2.59	2.6	2.61	2.64	2.61
ca	2.48	2.6	2.59	2.6	1.96	1.82	1.92
Smallest angle (deg.)	60	48.8	48.1	48.6	44.3	40.6	43.5
Mulliken charge (e) a	0.21	0.25	0.25	0.25	0.25	0.22	0.25
b	0.21	0.25	0.25	0.25	0	0	−0.01
c	0.22	0.05	0.03	0.04	0.27	0.23	0.27
Spin density (μ_B) a	−0.08	0.24	0.03	0.21	0.19	0.01	0.15
b	0.77	0.24	0.03	0.21	1.09	0.79	1.06
c	0.97	1.15	0.81	1.12	0.34	−0.17	0.28
a+b+c	1.66	1.63	0.87	1.54	1.62	0.63	1.49
Ribbon magnetism	Ferrimag.	Ferrimag.	Ferromag.	Ferrimag.	Ferrimag.	Ferromag.	Ferrimag.

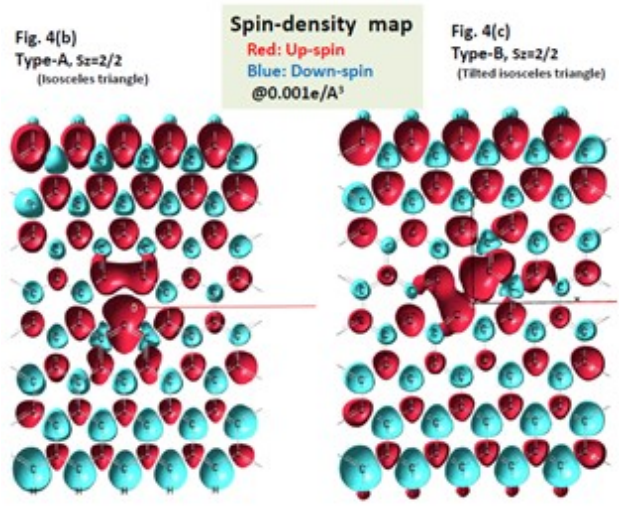

.

Fig. 4 Irregular up-spin cloud (by red) was observed at centered void triangle for both Type-A and -B. Inside of ribbon, there appear alternate up-spin (red) and down-spin (blue).

4. Curled ribbon

Amazing result was obtained in case of S_z=4/2 of Type-B as illustrated on Fig. 5(d), where appears a curled ribbon. While in case of S_z=2/2, ribbon is flat in (c). Void triangle of S_z=4/2 was 40.6degree comparing with 43.5 degree of S_z=2/2. The spin distribution is ferromagnetic like for S_z =4/2 as illustrated in Fig. 6(d). Both of upper and lower ribbon edges carry up-spin clouds. While in case of S_z=2/2 of Fig. 6(c), we can see anti-ferromagnetic like feature. It should be noted that energy of S_z=2/2 was -15.6kcal/mol., whereas S_z=4/2 was -15.5kcal/mol. They are only 0.1kcal/mol. difference. Such close energy suggests the coexistence both of flat ribbon and curled ribbon. Spin configuration of Fig 6(d) looks ferromagnetic like arrangement. Edge carbons are strongly magnetized by up-spins. However, it should be noted that each up-spins are isolated with neighbor edge spins. There is no exchange interaction between them. On the contrary, as studied in our previous paper on FeO-modified GNR[25], edge carbons were highly polarized by up-spins, and also coupled with neighbor edge spins by super-exchange interaction. It was usual ferromagnetic coupling. By such comparison, void induced GNR show unusual strongly polarized spin configuration, different with usual ferromagnetic one.

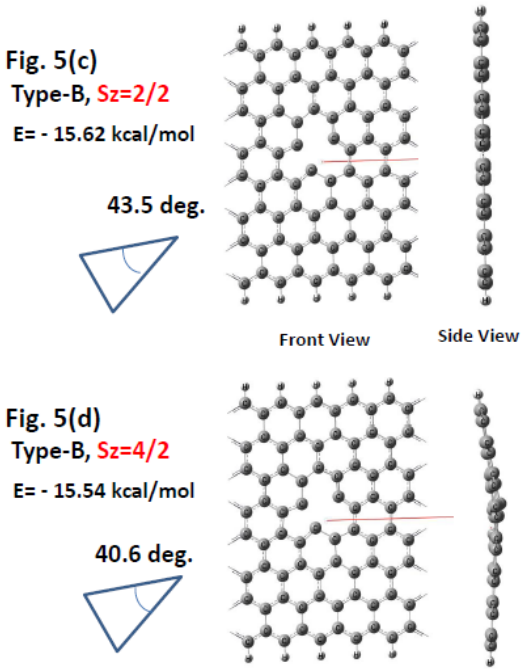

Fig. 5 In case of S_z=4/2 of Type-B, ribbon is curled as shown in (d), whereas for S_z=2/2 ribbon is flat (c).

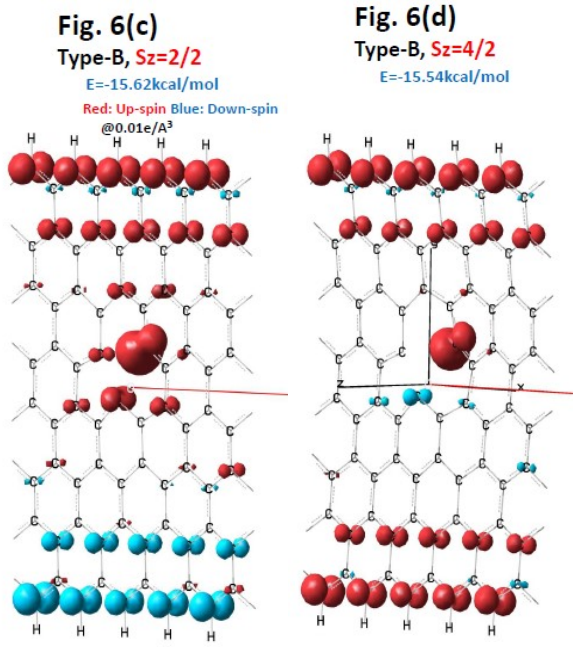

Fig. 6 In case of S_z=2/2 for Type-B, spin configuration is ferrimagnetic-like as shown in (c). Whereas in case of S_z=4/2, it is ferromagnetic-like (d).

5. Bi-layer GNR

To simulate three-dimensional graphite, bi-layered AB stacked GNR was analyzed. In Fig. 7, yellow marked atoms are surface (first) layer atoms including single void, whereas gray atoms are back (second) layer without any void. There are two types of void positions, which one is α-site void positioned over one carbon of the second layer (back side), whereas ß-site positioned over inter-atom space. Unit cell is [$C_{79}H_{10}$-$C_{80}H_{10}$]. Distance between two layers was calculated to be from 0.409 to 0.413nm depending on void situation as shown in Table 2. We can see deformed void triangle as classified by Type-A and Type–B as shown in Fig. 8. In every Type, the most stable spin state was S_z=2/2. Total energy of Type-B was lower (stable) than that of Type-A. Distorted triangle of Type-B shows small angle of 42degree compared with 53degree of Type-A. It should be noted that, in case of Type-B, total energy is almost similar for α-site (-14.59kcal/mol.) and ß-site (-14.69kcal/mol.). We can expect coexistence of both sites. Detailed results are summarized in Table 2. In Fig. 9, spin density of AB-stacked bi-layer GNR was illustrated. Spin density appeared only to the surface (first) layer. Back (second) layer shows no spin. Summed spin-density around one void was 1.37μB.

6. Comparison with experiments

6.1 Observation of void-defect

In 1998, Kerry et al.[14] observed void-defect on the surface of graphite by the scanning tunneling microscope. They observed triangle shape bright spot, which suggested large excess electrons inside of triangle void. Our calculation is consistent with such observation.

6.2 Observation of rotational symmetry of void defect

Notable result is the clockwise angle of a void triangle defined in the figure on bottom of Table 2. The clockwise angle θ of α-site void triangle was 300degree, whereas ß-site 240degree. There appear 60degrees rotation from ß-site to α-site. Such calculation is consistent with observation on graphite surface done by Ziatdinov et al.[16] using the scanning tunneling microscope.

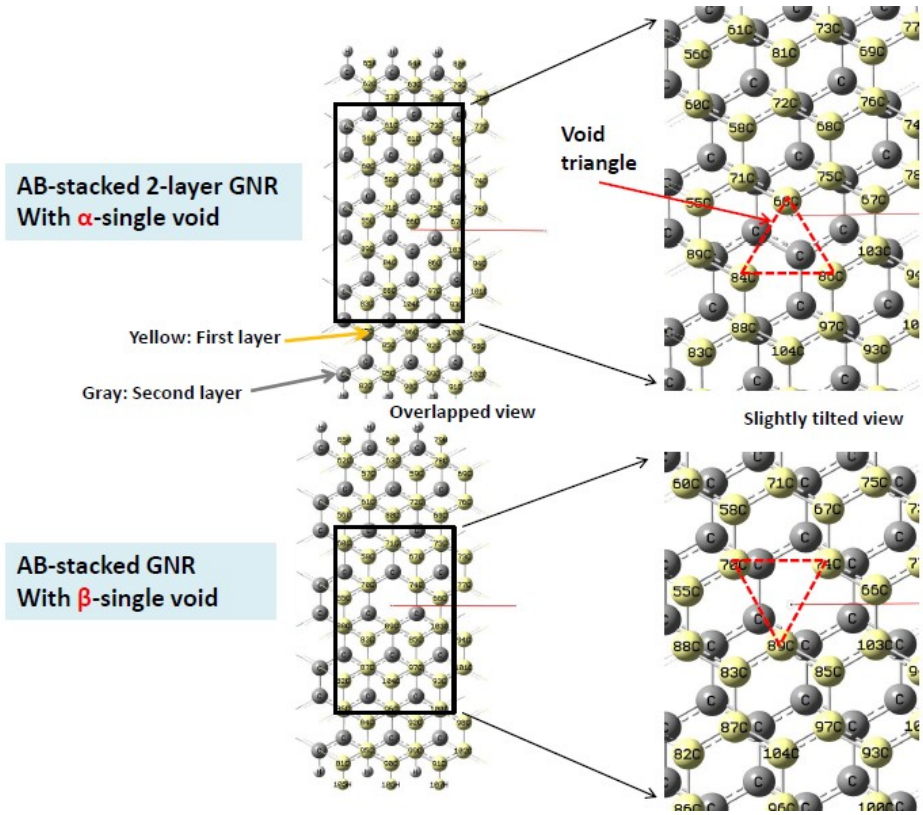

Fig. 7 Void-defect was created on AB-stacked bi-layer GNR with a void at α-site (top panel) and ß-site (bottom). Yellow atoms are surface layer carbon, whereas gray atoms back layer one.

Table 2 Calculated results of bi-layer GNR with single void. Cases are classified for Type-A or Type-B, and for void positions of α-site or ß-site.

Case number	Bi-initial	Alpha-A	Alpha-B	Beta-A	Beta-B
Void site	β	α	α	β	β
Distorted type	none	Type A	Type B	Type A	Type B
Given Sz	2/2	2/2	2/2	2/2	2/2
Stacked distance d (A)	4.1	4.09	4.11	4.13	4.11
Energy difference (kcal/mol/unit cell)	0	−13.33	−14.59	−12.61	−14.69
Ribbon configuration	Flat	Flat	Flat	Flat	Flat
Triangle distance ab (A)	2.45	2.63	2.64	2.34	2.53
bc	2.49	2.34	2.53	2.63	2.64
ca	2.49	2.63	1.84	2.63	1.84
Smallest angle (deg.)	60	52.8	41.7	52.8	41.7
Mulliken charge (e) a	0.22	0.04	0.21	0.21	0.24
b	0.22	0.21	−0.01	0.21	−0.01
c	0.17	0.21	0.24	0.04	0.21
Spin density (μ_B) a	0.33	0.9	0.04	0.25	0.25
b	0.34	0.25	1.08	0.25	1.08
c	0.84	0.25	0.25	0.9	0.04
Spin density (a+b+c)	1.51	1.4	1.37	1.4	1.37
Ribbon magnetism	Ferrimag.	Ferrimag.	Ferrimag.	Ferrimag.	Ferrimag.
Triangle vacancy tilt angle against GNR (θ)	0 deg.	180	300	0	240

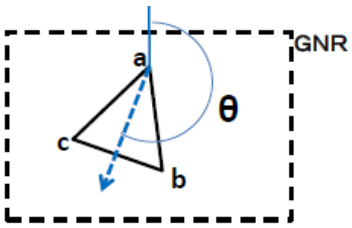

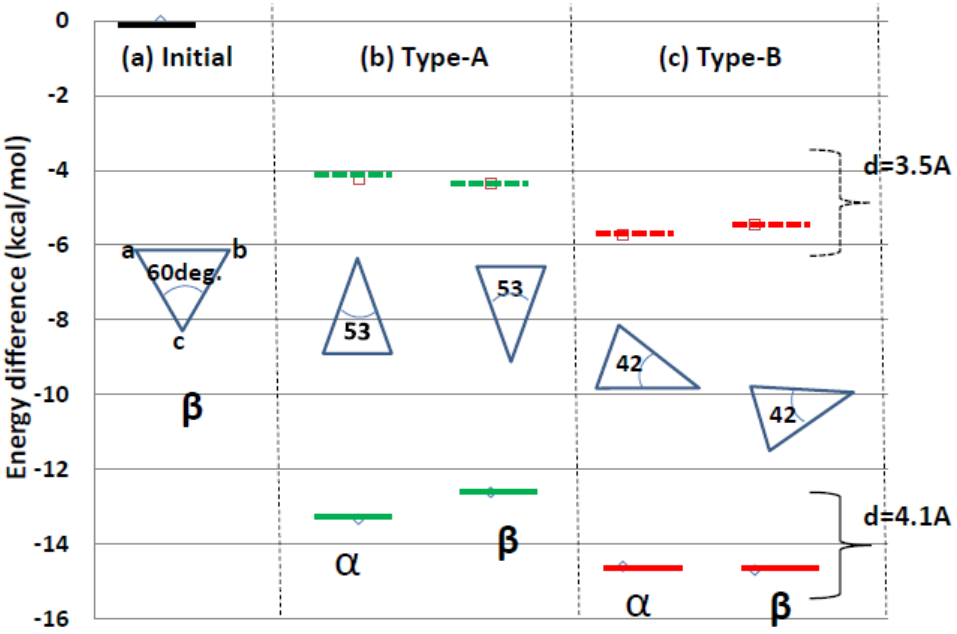

Fig. 8 Energy and void triangle are compared in AB-stacked bi-layer GNR.

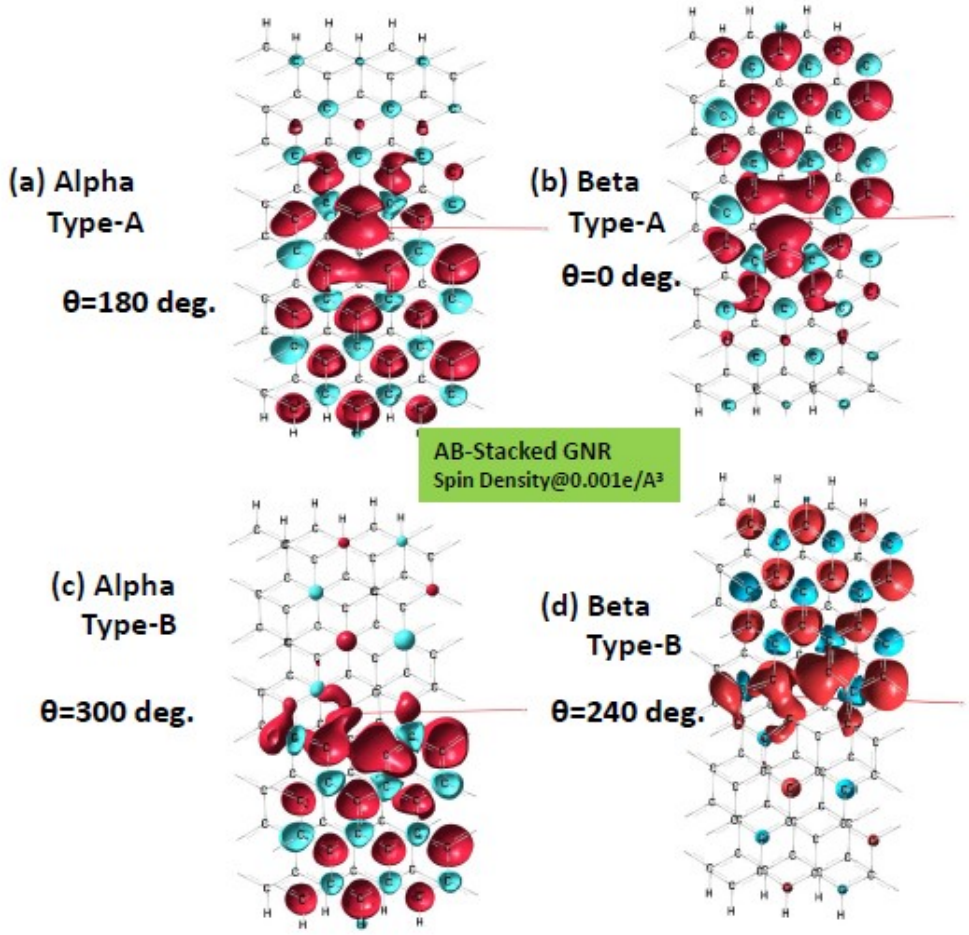

Fig.9 Spin density configuration of AB-stacked bi-layer GNR, where red cloud shows up-spin and blue one down-spin. Spin appears only to the surface layer. Back layer shows no spin.

7. Conclusion

Applying density functional theory to a void-defect in graphene-nano-ribbon (GNR), a relationship between multiple-spin-state and structure change was studied. An equilateral triangle of initial void was distorted to isosceles triangle due to re-bonding of excess six electrons in a void. Such calculation is consistent with actual observation by the scanning tunneling microscope. Six electrons enable the multiple spin-state of S_z=6/2, 4/2 and 2/2 due to the Hund's rule. The most stable spin state was S_z=2/2 showing flat ribbon structure. Amazing result was obtained for S_z=4/2, where ribbon was three dimensionally curled, and show ferromagnetic like spin distribution on both upper and lower edges of the ribbon. Energy of S_z=2/2 and S_z=4/2 were close, almost same. This suggests coexistence of flat and curled ribbon. As a model of three-dimensional graphite, bi-layered AB stacked GNR was analyzed for different void positions of α-site and ß-site. Both sites show similar energy. Void triangle presents 60 degrees clockwise rotation from ß-site to α-site. It should be noted that such void rotation coincides well with actual observation. This study revealed that void-defect in GNR induces unusual highly polarized spin state, different with usual ferromagnetic one.

References

1) P. Esquinazi, D. Spemann, R. Hohne, A. Setzer, K. Han, and T. Butz: *Phys. Rev. Lett.*, **91**, 227201 (2003).
2) K. Kamishima, T. Noda, F. Kadonome, K. Kakizaki and N. Hiratsuka: *J. of Mag. and Magn. Mat.*, **310**, e346 (2007).
3) T. Saito, D. Nishio-Hamane, S. Yoshii, and T. Nojima: *Appl. Phys. Lett.*, **98**, 052506 (2011).
4) Y. Wang, Y. Huang, Y. Song, X. Zhang, Y. Ma, J. Liang and Y. Chen: *Nano Letters*, **9**, 220 (2009).
5) J. Cervenka, M. Katsnelson and C. Flipse: *Nature Phys.,* **5**, 840 (2009), (https://doi.org/10.1038/nphys1399).
6) H. Ohldag, P. Esquinazi, E. Arenholz, D. Spemann, M. Rothermal, A. Setzer, and T.Butz: *New Journal of Physics*, **12**, 123012 (2010).
7) J. Coey, M. Venkatesan, C. Fitzgerald, A. Douvalis and I. Sanders: *Nature*, **420**, 156 (2002).
8) K. Kusakabe and M. Maruyama: *Phys. Rev. B*, **67**, 092406 (2003).
9) N. Ota, N. Gorjizadeh and Y. Kawazoe: *J. Magn. Soc. Jpn.*, **36**, 36 (2012).
10) N. Ota: *J. Magn. Soc. Jpn.*, **37**, 175 (2013).
11) P. Lehtinen, A. Foster, Y. Ma, A. Krasheninnikov, and R. Nieminen: *Phys. Rev. Lett.*, **93**, 187202 (2004).
12) P.Ruffieux, O. Groning, P. Schwaller, L. Schlapbach, and P. Groning: *Phys. Rev. Lett.*, **84**, 4910 (2000).
13) A. Hashimoto, K. Suenaga, T. Sugai, H.Shinohara, and S. Iijima: *Nature (London)*, **430**, 870 (2004).
14) K.Kelly and N.Hales: *Surface science*, **416**, L1085 (1998).
15) T. Kondo, Y. Honma, J. Oh, T. Machida, and J. Nakamura: *Phys. Rev. B*, **82**, 153414 (2010).
16) M. Ziatdinov, S. Fujii, K. Kusakabe, M. Kiguchi, T. Mori, and T. Enoki: *Phys. Rev. B,* **89**, 155405 (2014).
17) O. Yazyev and L. Helm: *Phys.Rev. B*, **75**, 125408 (2007).
18) B. Wang and S. Pantelides: *Phys. Rev. B*, **86**, 165438 (2012).
19) P. Hohenberg and W. Kohn: *Phys. Rev.*, **136**, B864 (1964).
20) W. Kohn and L. Sham: *Phys. Rev.*, **140**, A1133(1965).
21) J. P. Perdew, K. Burke and M. Ernzerhof: *Phys. Rev. Lett.*, **77**, 3865(1996).
22) M. Frisch, G. Trucks, H. Schlegel et al.: Gaussian 03 package software, Gaussian Inc. Wallington CT USA (2009).
23) R. Ditchfield, W. Hehre and J. Pople: *J. Chem. Phys.*, **54**,724 (1971).
24) F. Hund: *Z. Phys.*, **33**, 345 (1923).
25) N. Ota: *J. Magn. Soc. Jpn.*, 38, 107-110 (2014).

Received Oct. 25, 2020; Accepted Jun.12, 2021

J. Magn. Soc. Jpn., **45**, 37-40 (2021)

<Paper>

Anomalous Nernst and Seebeck effects in $NiCo_2O_4$ films

Hiroki Koizumi, Atsushi Hidaka, Takashi Komine*, and Hideto Yanagihara**
Department of Applied Physics, University of Tsukuba, Tsukuba,*1-1-1 Ten-nodai, Tsukuba, Ibaraki 305-8573, Japan*
*Graduate School of Science and Engineering, Ibaraki University,*4-12-1 Nakanarusawa, Hitachi, Ibaraki 316-8511, Japan*
**Tsukuba Research Center for Energy Materials Science (TREMS), University of Tsukuba,*1-1-1 Ten-nodai, Tsukuba, Ibaraki 305-8573, Japan*

We investigated both the Seebeck and anomalous Nernst effects in $NiCo_2O_4$(001) epitaxial films with a preferential magnetization direction normal to the film plane. Since the thermoelectric signals were extremely small, we custom-built a measurement system to detect the weak voltage signals. To suppress spurious voltage signals originating from the electrical contacts in the measurement circuit, we employed the following measures. We reduced the number of electrical contacts between the output of a commercial cryostat with a superconducting magnet and the nano-voltmeters. We employed silver soldering while making the electrical contacts to reduce the thermal electromotive force voltages at the remaining contacts. By adopting these measures, we have succeeded in detecting thermoelectric voltages as small as 5 nV. The observed thermoelectric efficiency of $NiCo_2O_4$ is quite small compared to conventional ferromagnetic metals.

Key words: $NiCo_2O_4$, Anomalous Nernst effect, Perpendicular magnetic anisotropy

1 Introduction

In the recent past, different types of energy conversion technologies have been studied due to the increasing need for alternative and sustainable energy sources [1,2]. Among the energy conversion technologies, the thermoelectric device has received much attention as it enables the direct conversion of waste heat energy into electrical energy [3,4]. Moreover, thermoelectricity is interesting from the perspective of condensed matter physics because it depends on the electrical and thermal transport phenomena, which are intrinsically related to the electronic state of materials. Particularly in magnetic materials, the temperature gradient can be converted into electrical voltage through thermomagnetic phenomena, such as the anomalous Nernst effect (ANE) and the spin Seebeck effect [5,6]. Another transport phenomenon as a counterpart of ANE is known anomalous Hall effect (AHE). Both the AHE and ANE reflect well the electronic state of materials, they have contributions from the extrinsic and intrinsic mechanisms [3,7,8]. However, since the electric field generated by ANE is smaller than AHE one's, it hinders to investigate the relation between thermal and electrical transport in various materials. Therefore, for understanding the electronic state of materials by ANE, a measurement system that can detect the weak thermoelectric voltage desired.

The ANE is defined as the generation of an electric field ($\boldsymbol{E}_{\mathrm{ANE}}$) along the direction of the outer product of the magnetization ($\boldsymbol{M}$) and the temperature gradient (∇T). Thus, it is experimentally observed as an anomalous transverse voltage [9]. For example, in the case of ∇T and $\boldsymbol{M}$ parallel to x- and z-axis respectively, $\boldsymbol{E}_{\mathrm{ANE}}$ appears along the y-axis direction. In other words, ANE in a magnetic material with perpendicular magnetic anisotropy (PMA) could generate a large thermoelectric voltage by expanding the area in the vertical direction from the temperature gradient. Therefore, PMA can be a crucial factor for generating large ANE voltage [3,10].

Oxide-based thermoelectric materials have many advantages such as the following: they are non-toxic and non-polluting; they can be synthesized in the air and do not need inert conditions or vacuum; they are stable even at high temperatures. These advantages make oxide thermoelectric materials a potential candidate for practical applications at elevated temperatures. As a candidate oxide thermoelectric material with PMA, we focused on $NiCo_2O_4$(NCO). NCO has an inverse spinel-type structure ($Fd\bar{3}m$) and is a conductive ferrimagnet with a high transition temperature ($T_C \approx 400$ K) [11]. Further, some previous studies reported that NCO has mixed-valence cations and can be expressed by a general formula, $Co^{2+}_x Co^{3+}_{1-x}[Co^{3+}Ni^{2+}_{1-x}Ni^{3+}_x]O^{2-}_4$ ($0 < x < 1$), where tetrahedral (T_d) site is occupied by high spin Co^{2+} (d^7, $S = 3/2$) and Co^{3+} (d^6, $S = 3/2$), octahedral (O_h) site is occupied by low spin Ni^{2+} (d^8, $S = 1$), Ni^{3+} (d^7, $S = 1/2$), and diamagnetic low spin Co^{3+} (d^6, $S = 0$). The saturation magnetic moment is 2 μ_B/f.u. irrespective of x. It has been reported that in the presence of such a large number of states in the system , a large thermoelectric signal can be generated via an increase in entropy [12,13]. In addition, NCO film grown on the $MgAl_2O_4$ (MAO) substrate exhibits strong PMA [14,15], which is approximately 0.3 MJ/m^3 at room temperature for a -0.3% epitaxial strain. A recent theoretical investigation showed that Co at the T_d site is responsible for PMA [16].

In this study, we designed a measurement system to detect the weak thermoelectric voltage signal and investigated the thermoelectric properties of NCO. This manuscript is organized as follows. Sample preparation and design of the measurement setup are explained in Section 2. We present experimental results and discussion in Section 3 and summarize the work in the final section.

2 Experiment

2.1 Sample preparation

Epitaxial NCO thin films with a thickness of 50 nm were grown by reactive radio frequency magnetron sputtering technique (ES-250MB: Eiko Engineering Co.,Ltd.)[17–19]. We used a 2-inch alloy target with the ideal composition of Ni:Co= 1 : 2. Before growing the film, a single crystal MAO substrate was ultrasonically degreased using acetone, ethanol, and deionized water for 5 min at each step. The growth conditions of NCO thin films were as follows: Ar and O_2 flow rates were set to 10 and 2.5 sccm, respectively; the process temperature was 300°C, and the working pressure was 1.3 Pa. Thereafter, we annealed the NCO films at 300°C for 30 min under an oxygen pressure of 0.2 Pa [20]. The film structure was characterized by reflection high-energy electron diffraction (RHEED), X-ray reflectivity (XRR, by Rigaku Smart Lab, using Co $K\alpha_1$ radiation), and X-ray diffraction (XRD). Magnetic hysteresis (MH) loops were measured by a vibrating sample magnetometer (VSM) option of the Physical Property Measurement System (PPMS) from Quantum Design.

2.2 Measurement setup

To perform the thermoelectric measurements, we designed and built a sample holder, as illustrated in FIG. 1. Figure 1 shows schematic illustrations of the sample holder. The sample was bridged on the top of two Cu plates ($5\times13\times1$ mm^3 and $5\times13\times3$ mm^3). The one Cu plate was directly placed on the sample holder (P102/3A, Quantum Design), where the temperature was measured using the PPMS system. The another Cu plate was placed on the sample holder through Bakelite®($5\times13\times2$ mm^3) for thermal insulation. Moreover, a chip resistor (R = 330 Ω, TE Connectivity, 3522330RFT) acting as a heater was attached to this side to raise the temperature. Here, the electrodes on the back of the chip resistor were removed by polishing. Input electric power was supplied to the chip resistor using a source meter (Keithley2400). To monitor the actual temperature difference between the Cu plates, we fabricated a type-E thermocouple from chromel (TFCH-003) and constantan (TFCC-003), supplied by Omega Engineering Inc. The thermal contact between the thermocouple and each Cu plate was made using GE7031 varnish via a small piece of thin paper. The thermal electromotive force (TEMF) of the thermocouple was measured by a voltmeter (Keithley196) and converted into the temperature difference (ΔT) using the reference table [21]. In the designed holder, the distance between the two Cu plates is ℓ = 4 mm. Therefore, the temperature gradient is expressed as $\nabla T \approx \Delta T/\ell$. The typical width of the sample is w = 3 mm. Note that we have confirmed the error between the actual temperature difference of the two Cu plates and the output of the thermocouple is less than 5%.

Next, the film was patterned by the photolithography technique, and Cr and Au were sputtered as the electrodes. Four electrodes were deposited on the top of the films for thermoelectric measurement as illustrated in Fig.1. Two electrodes placed along the thermal gradient are for measuring the Seebeck signal (V_{xx}), and the other two are for measuring the ANE signal (V_{xy}). Here, a point contact electrode was fabricated to prevent a decrease in TEMF [22]. The sample was cut into a rectangular shape (5×10 mm^2) to place it on the sample holder and was glued by GE7031 varnish. We used aluminum wires for making connections between electric pads and the sample puck. One side of the sample was heated, and ∇T was induced along the long side of the rectangle. The voltage induced along the long side (V_{xx}) was measured as a Seebeck voltage using Channel 2 of Keithley 2182, and the voltage induced across the long side (V_{xy}) was measured as a Nernst signal using Channel 1 of Keithley 2182. For ANE measurements, a magnetic field perpendicular to the sample plane was applied. Further, to reduce the number of electrical contacts, we fabricated a signal cable to directly connect above measurement instruments and output connectors of PPMS. In the sample holder and the cable, we used silver soldering at all electrical contact points to reduce contact voltages.

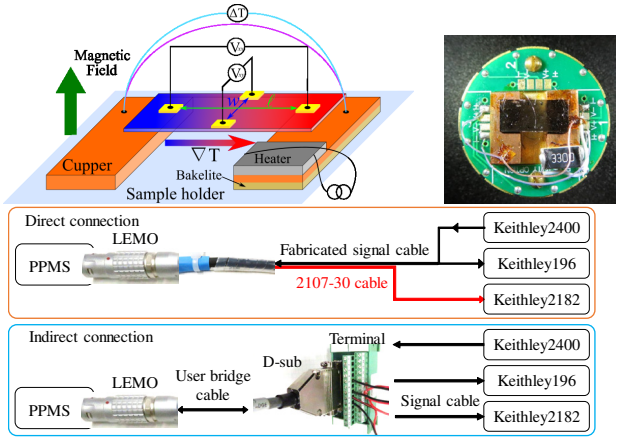

Fig. 1 Structure of the sample holder and configuration for measuring thermoelectric properties. Left panel shows schematics of the sample setup, and right panel represents the top view of the sample puck. Bottom panel shows block diagram of indirect and direct connection cable.

3 Results and discussion

3.1 Structural characterization

Figures 2 (a)-(d) show the XRD patterns with scattering vector $\boldsymbol{k}$ parallel to MAO[001], [100], and [110], respectively. The dashed lines indicate the diffraction angles expected for the bulk MAO. All the observed Bragg peaks can be consistently assigned to a spinel structure. In Figs. 2 (b)-(d), reflections were only confirmed at the Bragg peak positions on the MAO substrate. This result implies that NCO film has epitaxial distortion, and its lattice constants are a = 8.08 Å and c = 8.27 Å. Based on the lattice constant of NCO (a_{NCO} = 8.10 Å)[11] and MAO (a_{MAO} = 8.08 Å) in bulk, NCO thin films experience a compressive strain of

~ 0.3% due to the lattice mismatch. These results are consistent with the previous studies [14–16,20,23].

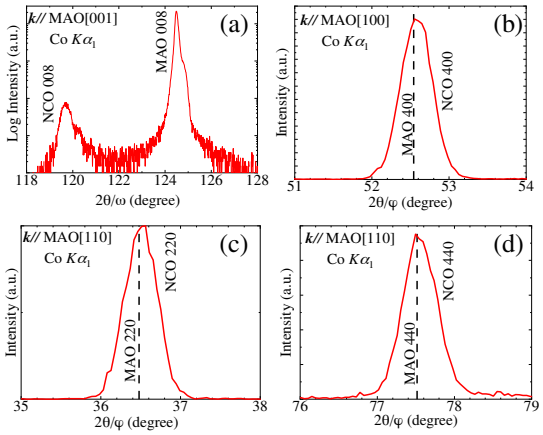

Fig. 2 X-ray diffraction patterns of the scattering vector $\boldsymbol{k}$ parallel to (a)[001], (b)[100], and (c-d)[110], respectively .

3.2 Thermoelectric properties

First, we show the effect of reducing the number of electrical connections on the measurement system. We tested two different ways of connecting the 14-pins LEMO connector(FGG.3B.314.CLAD92) of the interface of the cryostat of PPMS to the nanovolt-meters; (1) the interface was wired to the instruments using regular LEMO-D-sub cable with an electric terminal(indirect connection), (2) the interface was directly connected to the instruments using the home-built cable as explained in Section 2 (direct connection). Figure 3 (a) shows the time dependence of the measured signals V_{xy} for $\Delta T = 0$.

In the case of an indirect connection set up, one can see periodically oscillating $\approx 1\ \mu$V of spurious voltage signals, probably because of the change in the temperature in the laboratory due to the air conditioner. In contrast, in the case of the direct connection set up, the periodically varying spurious voltage signal was suppressed, and the standard deviation was approximately 5 nV. This result indicates that thermoelectric voltages generated at the electrical connections of the measurement system could be a serious problem while measuring weak DC voltage signals.

Using the direct connection setup, we investigated the thermoelectric properties of the sample. Figure 3 (b) shows ΔT dependence of the Seebeck voltage (V_{xx}) at 300 K. A single data point represents the average voltage for approximately 5 min after generating a stable ΔT. The relative Seebeck coefficient (S_{xx}) between NCO and the Al wire is expressed as,

$$S_{xx} = \frac{E_{xx}}{\nabla T} = \frac{V_{xx}/\ell}{\Delta T/\ell} = \frac{V_{xx}}{\Delta T}. \tag{1}$$

Thus, from the slope of this figure, we can determine S_{xx}, which is 6.4 μV/K. From Ref.24, excluding absolute Seebeck coefficient of the Al, the absolute Seebeck coefficient of the NCO(S_{xx}^{NCO}) can be estimated, which is 8.0 μV/K at 300 K. Table 1 shows the temperature dependence of S_{xx}^{NCO}, which decreases as the temperature decreases.

Table 1 Temperature dependence of absolute Seebeck coefficient (S_{xx}^{NCO}) and anomalous Nernst coefficient (S_{xy}^{NCO}).

Temperature (K)	S_{xx}^{NCO} (μV/K)	S_{xy} (μV/K)
100	2.8	−0.005
200	3.6	−0.030
300	8.0	−0.035

Next, we describe the results of the ANE measurement of NCO. Figure 3 (c) shows the time dependence of V_{xy} from powering up the heater to measurement start. In this measurement, the input power is controlled to be $\Delta T \approx 10$ K ($I \approx 25$ mA) and 50 times averages are taken per point, which takes about 15 minutes from the beginning to the end. From Fig. 3 (c), while above 200 K, V_{xy} is stable after elapsing 5 min at least; at 100 K, more than 20 min are needed for the TEMF voltage to become stable. These results may imply that a new path for thermal diffusion appears at low temperatures. Before we start the ANE measurement, we need to wait for a sufficient duration for the V_{xy} to become stable. S_{xy} is determined from the experimentally measured voltages as follows:

$$S_{xy} = \frac{E_{xy}}{\nabla T} = \frac{V_{xy}/w}{\Delta T/\ell}, \tag{2}$$

where $w = 3$ mm, $\ell = 4$ mm. Figure 3 (d) shows the S_{xy}-H loop at each temperature. Here, the time dependent background component expected from Fig. 3(a) is smaller than the ANE voltage at each temperatures. In ANE analysis, we extracted only the odd function components, similar to that in the analysis performed for the Hall effect. The shape of the S_{xy}-H loop is in good agreement with a previously reported VSM measurement result (not shown) [25]. Moreover, a larger saturated S_{xy} appeared at higher temperatures. From Ref.26, the relation between Nernst and Seebeck coefficient can be written as follow,

$$S_{xy} \simeq S_{xx} \tan\theta_H + \rho_{xx}\epsilon_{yx}, \tag{3}$$

where θ_H is Hall angle, ρ_{xx} is longitudial resistivity, and ϵ_{yx} is off-diagonal element of the thermoelectric tensor. In NCO, $\theta_H \sim -10^{-3}$ and $\rho_{xx} \sim 10^{-3}$ Ωcm [14]. Therefore, the expected S_{xy} from S_{xx} is approximately 0.01 μV/K, which is almost same with the experimental results. The little difference may be attributed to the thermoelectric tensor.

4 Conclusion

In this study, we investigated both the Seebeck effect and ANE in $NiCo_2O_4$thin films with PMA. The thermoelectric signals are extremely small that we needed to build a measurement system to detect the weak thermoelectric voltage signals. To suppress the spurious voltage signals originating from the electrical contacts at room temperature of the measurement system, we employed the

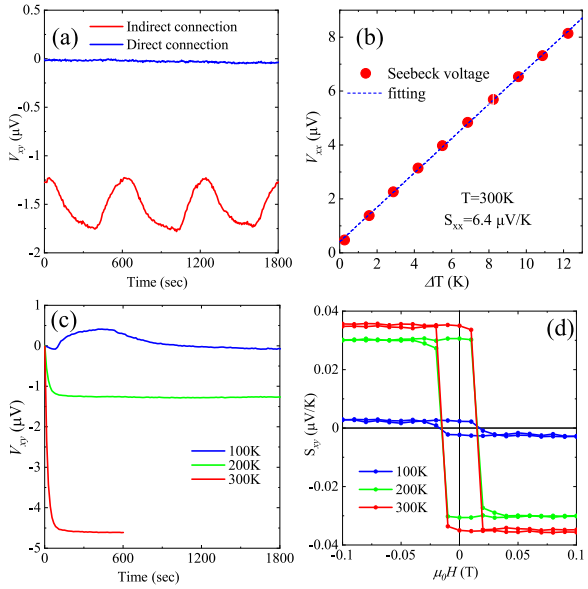

Fig. 3 (a) Comparison of the connection methods between the sample chamber and the measurement instruments. (b) ΔT dependence of relative Seebeck voltage (V_{xx}) at 300 K. (c) Time dependence of V_{xy} from power input to measurement start. (d) Temperature dependence of anomalous Nernst coefficient S_{xy}.

following solutions: (i) reduction in the number of electrical contacts by directly connecting the output of a commercial cryostat with a superconducting magnet to the nano-voltmeters, (ii) used silver soldering to make electrical contacts to reduce contact voltages. By adopting the aforementioned measures, we succeeded in detecting thermoelectric voltages as small as 5 nV.

Acknowledgments This project is partly supported by Japan Science and Technology Agency (JST) under collaborative research based on industrial demand "High Performance Magnets: Towards Innovative Development of Next Generation magnets" (JP-MJSK1415), KAKENHI(19KK0104) , the Ibaraki University-Tsukuba Joint Coordination Fund, and the Tanigawa Fund Promotion of Thermal Technology. This work was performed under the approval of the "Photon Factory Program Advisory Committee" (proposals No.2017G602 and No. 2016S2-005). H. K. acknowledges the "Kato Foundation for Promotional Science". H. K. acknowledges support of Grant-in-Aid for JSPS Fellows (20J10749). H. K. thanks K. Toko for providing a reference sample that has a large Seebeck coefficient.

References

1) David Griggs, Mark Stafford-Smith, Owen Gaffney, Johan Rockström, Marcus C. Öhman, Priya Shyamsundar, Will Steffen, Gisbert Glaser, Norichika Kanie, and Ian Noble. *Nature*, **495**, 305 (2013).
2) Will Steffen, Katherine Richardson, Johan Rockström, Sarah E. Cornell, Ingo Fetzer, Elena M. Bennett, Reinette Biggs, Stephen R. Carpenter, Wim de Vries, Cynthia A. de Wit, Carl Folke, Dieter Gerten, Jens Heinke, Georgina M. Mace, Linn M. Persson, Veerabhadran Ramanathan, Belinda Reyers, and Sverker Sörlin. *Science*, **347**, 736 (2015).
3) Akito Sakai, Susumu Minami, Takashi Koretsune, Taishi Chen, Tomoya Higo, Yangming Wang, Takuya Nomoto, Motoaki Hirayama, Shinji Miwa, Daisuke Nishio-Hamane, Fumiyuki Ishii, Ryotaro Arita, and Satoru Nakatsuji. *Nature*, **581**, 53 (2020).
4) Akihiro Kirihara, Koichi Kondo, Masahiko Ishida, Kazuki Ihara, Yuma Iwasaki, Hiroko Someya, Asuka Matsuba, Ken-ichi Uchida, Eiji Saitoh, Naoharu Yamamoto, Shigeru Kohmoto, and Tomoo Murakami. *Scientific Reports*, **6**, 23114 (2016).
5) Walther Nernst. *Annalen der Physik*, **267**, 760 (1887).
6) K. Uchida, S. Takahashi, K. Harii, J. Ieda, W. Koshibae, K. Ando, S. Maekawa, and E. Saitoh. *Nature*, **455**, 778 (2008).
7) Naoto Nagaosa, Jairo Sinova, Shigeki Onoda, A. H. MacDonald, and N. P. Ong. *Review of Modern Physics*, **82**, 1539 (2010).
8) Di Xiao, Ming-Che Chang, and Qian Niu. *Review of Modern Physics*, **82**, 1959 (2010).
9) Gerrit E. W. Bauer, Eiji Saitoh, and Bart J. van Wees. Spin caloritronics. *Nature Materials*, **11**, 391 (2012).
10) Amilcar Bedoya-Pinto, Marco Donolato, Marco Gobbi, Luis E. Hueso, and Paolo Vavassori. *Applied Physics Letters*, **104**, 062412 (2014).
11) P.D. Battle, A.K. Cheetham, and J.B. Goodenough. *Materials Research Bulletin*, **14**, 1013 (1979).
12) I. Terasaki, Y. Sasago, and K. Uchinokura. *Physical Review B*, **56**, R12685 (1997).
13) W. Koshibae, K. Tsutsui, and S. Maekawa. *Physical Review B*, **62**, 6869 (2000).
14) Xuegang Chen, Xiaozhe Zhang, Myung-Geun Han, Le Zhang, Yimei Zhu, Xiaoshan Xu, and Xia Hong. *Advanced Materials*, **31**, 1805260 (2019).
15) Daisuke Kan, Masaichiro Mizumaki, Miho Kitamura, Yoshinori Kotani, Yufan Shen, Ikumi Suzuki, Koji Horiba, and Yuichi Shimakawa. *Physical Review B*, **101**, 224434 (2020).
16) Corbyn Mellinger, Jace Waybright, Xiaozhe Zhang, Caleb Schmidt, and Xiaoshan Xu. *Physical Review B*, **101**, 014413(2020).
17) Hiroki Koizumi, Sonia Sharmin, Kenta Amemiya, Masako Suzuki-Sakamaki, Jun-ichiro Inoue, and Hideto Yanagihara. *Physical Review Materials*, **3**, 024404 (2019).
18) Hiroki Koizumi, Jun-ichiro Inoue, and Hideto Yanagihara. *Physical Review B*, **100**, 224425 (2019).
19) Hiroki Koizumi, Michio Hagihara, Soki Kobayashi, and Hideto Yanagihara. *AIP Advances*, **10**, 015108 (2020).
20) Ikumi Suzuki, Daisuke Kan, Miho Kitamura, Yufan Shen, Koji Horiba, and Yuichi Shimakawa. *Journal of Applied Physics*, **127**, 203903 (2020).
21) G.W. Burns, National Institute of Standards, and Technology (U.S.). NIST monograph ; 175. U.S. Dept. of Commerce, National Institute of Standards and Technology ; For sale by Supt. of Docs., U.S. G.P.O, Gaithersburg, MD : Washington, 1993. "Supersedes NBS monograph 125.".
22) Ryo Ando and Takashi Komine. *AIP Advances*, **8**, 056326 (2018).
23) Yufan Shen, Daisuke Kan, Zhenhong Tan, Yusuke Wakabayashi, and Yuichi Shimakawa. *Physical Review B*, **101**, 094412 (2020).
24) Ronald J. Gripshover, John B. VanZytveld, and Jack Bass. *Physical Review*, **163**, 598 (1967).
25) Hiroki Koizumi and Hideto Yanagihara. Manuscript in preparation
26) Ryo Ando, Takashi Komine, and Yasuhiro Hasegawa. *Journal of Electronic Materials*, **45**, 3570 (2016).

Recieved Oct. 30, 2020; Revised Dec. 21, 2020; Accepted Jan. 15, 2021

J. Magn. Soc. Jpn., **45**, 41-49 (2021)

<Paper>

Void-Defect Induced Magnetism and Structure Change of Carbon Material- Ⅱ : Graphene Molecules

Norio Ota[1], Aigen Li[2], Laszlo Nemes[3] and Masaaki Otsuka[4]

[1]Graduate school of Pure and Applied Sciences, University of Tsukuba, *1-1-1 Tennodai, Tsukuba-City Ibaraki, 305-8571, Japan*

[2]Department of Physics and Astronomy, University of Missouri, *Columbia, MO 65211, USA*,

[3]Research Center for Natural Sciences, Ötvös Lóránd Research Network, *Budapest 1519, Hungary*

[4]Okayama Observatory, Kyoto University, *Asakuchi Okayama, 719-0232, Japan,*

Void-defect is a possible origin of ferromagnetic feature on pure carbon materials. In our previous paper, void-defect on graphene-nanoribbon show highly polarized spin configuration. In this paper, we studied cases for graphene molecules by quantum theory, by astronomical observation and by laboratory experiment. Model molecules for the density functional theory are graphene molecules of C_{23} and C_{53} induced by a void-defect. They have carbon pentagon ring within a hexagon network. Single void has three radical carbons, holding six spins. Those spins make several spin-states, which affects to molecular structure and molecular vibration, finally to infrared spectrum. The stable spin state was triplet, not singlet. This suggests magnetic pure carbon molecule. It was a surprise that those molecules show close infrared spectrum with astronomically observed one, especially observed on carbon rich planetary nebulae. We could assign major band at 18.9 micrometer, and sub-bands at 6.6, 7.0, 7.6, 8.1, 8.5, 9.0 and 17.4 micrometer. Also, calculated spectrum roughly coincides with that of laboratory experiment by the laser-induced carbon plasma, which is an analogy of cosmic carbon creation in interstellar space.

Key words: graphene, void, spin state, DFT, planetary nebula, infrared spectrum

1. Introduction

Graphene and graphite like carbon materials are candidates for showing ferromagnetic like hysteresis[1)-6)]. There are many capable explanations based on impurities[7)], edge irregularities[8)-10)] or defects[11)-16)]. The density functional theory (DFT) shows good coincidence with experiments[17)-19)] and revealed reasonable consistency with several fundamental theories[20)-21)]. Despite such many efforts, origin of magnetic ordering could not be thoroughly understood. Our previous study on graphene nano-ribbon (GNR) revealed that void-defect brings unusual highly polarized spin configuration and structure change, which will be opened in this journal under the same title as number -I. In this paper, we like to apply our study to graphene molecules, smaller than GNR. Unfortunately, on laboratory experiment, small pure carbon molecule does not show any magnetic feature. The reason may be molecule-to-molecule interaction at high density (10^{10}~10^{23} molecules/cm^3) conditions on earth. Radical carbon's magnetic feature in small molecules may be cancelled out by complex interaction between molecules. Now, we should look at astronomical carbon dust floating in interstellar and circumstellar space. Molecules are kept under peculiar condition of ultra-low density (1~100 molecules/cm^3), almost no interaction each other. Molecular structure affects molecular vibration and infrared spectrum. In this study, calculated infrared spectrum will be compared with the astronomically observed one, also with the laboratory experiment of the laser induced carbon plasma.

Fullerene C_{60} was discovered by Kroto et al.[22)] (the 1996 Nobel Prize) in the sooty residues of vaporized carbon. They already suggested that "fullerene may be widely distributed in the universe". The presence of C_{60} in astrophysical environments was revealed by the detection of a set of emission bands at 7.0, 8.45, 17.3 and 18.9 μm[23)-27)]. Typical astronomical objects are the Galactic planetary nebula (PNe) Tc1[23)] and the Small Magellanic Cloud Lin49[28)]. Observed spectra were compared with experiment and theory[23)29)-31)]. However, there remain undetermined observed bands, not be explained by C_{60}.

It is well known that graphene is a raw material for synthesizing fullerene[32)33)]. By observation of Lin49, Otsuka et al.[28)] suggested the presence of small graphene. Graphene was first experimentally synthesized by Geim and Novoselov[34)] (the 2010 Nobel Prize). The possible presence of graphene in space was reported by Garcia-Hernandez et al.[35)-37)]. These infrared features appear to be coincident with planar C_{24} having seven carbon hexagon rings. However, full observed bands still cannot be explained by C_{24} or hexagon network molecules[38)]. Some hints come from carbon SP3 defect among SP2 network caused by single void-defect in carbon hexagon network by Ota[39)]. Also, Galue & Leines[40)] predicted the physical model supposing pi-electron irregularity. In this paper, we

apply one assumption of single void-defect on graphene molecule. At the first part, DFT calculation will be applied to model molecules. Void position discriminates detailed molecule species. Spin dependent calculation will be done to obtain detailed molecular structure and molecular vibrational infrared spectrum. At the second part, we will compare such calculated spectra with astronomically observed one. Finally, we like to compare with laboratory experiment of laser induced carbon plasma spectrum[41)42)], which will be an analogy of cosmic carbon creation in space.

2. Model Molecules and Calculation Method

Model molecules are illustrated in Fig. 1 starting from C_{24} having seven carbon hexagon rings[35)]. To find size dependence, we add larger one of C_{54}. In this paper, we apply one assumption of single void-defect on such initial molecules. In laboratory experiment, high speed particle can create such void. Similarly, in astronomical space, the cosmic ray as like proton may attack graphene[35-37)]. As illustrated on top left of Fig. 1, high speed particle attacks graphene and kick out one carbon atom. DFT calculation shows molecular configuration of void-defect induced graphene molecules as like C_{23}, and C_{53}, which have one pentagon ring among hexagon networks. Molecular structure depends on the void position as marked by a, b, c, d, e, f, in left of Fig. 1. Void induced molecule species is named by suffixing a, b, and so on, such as (C_{23}-a) and (C_{23}-b). Molecular energy of (C_{23}-a) is 1.04 eV higher than that of (C_{23}-b). In this study, we supposed isolate molecule, which means no molecule-to-molecule interaction, and no energy competition between different void induced species. While we need energy competition between spin states for every individual species. It should be noted that one void has 3 radical carbons and holds 6 spins. Such spins bring spin-multiplicity, which affect to molecular structure and molecular vibration, finally to infrared spectrum.

In calculation, we used DFT[43) 44)] with the unrestricted B3LYP functional[45)]. We utilized the Gaussian09 software package[46)] employing an atomic orbital 6-31G basis set[47)]. Unrestricted DFT calculation was done to have the spin dependent atomic structure. The required convergence of the root-mean-square density matrix was 10^{-8}. Based on such optimized molecular configuration, fundamental vibrational modes were calculated, such as C-C stretching modes, C-C bending modes and so on, using the Gaussian09 software package. This calculation also gives harmonic vibrational frequency and intensity in infrared region. The standard scaling is applied to the frequencies by employing a scale factor of 0.975 for pure carbon system taken from the laboratory experimental value of 0.965 based on coronene molecule of $C_{24}H_{12}$[39)]. Correction due to anharmonicity was not applied to avoid uncertain fitting parameters. To each spectral line, we assigned a Gaussian profile with a full width at half maximum (FWHM) of $4cm^{-1}$.

3. Spin State Analysis and Structure Change

We tried the multiple spin-state analysis. Example is shown in Fig. 2 for spin state of S_z=2/2 of (C_{23}-a) and (C_{23}-b). In this study, we dealt total molecular spin $\boldsymbol{S}$ (vector). Molecule is rotatable material, easily follows to the external magnetic field of z-direction. Projected component to z-direction is maximum value of S_z, which is good quantum parameter. In molecular magnetism, S_z=2/2 is named as triplet spin-state. Initial void-defect holds 3 radical carbons and allows 6 spins as illustrated in left. Six spins make capable spin-states of S_z=0/2, 2/2, 4/2 and 6/2. Among them, calculated energy of S_z=4/2 and 6/2 resulted unstable high energy. Here, we like to compare cases of S_z=0/2 and 2/2. One radical carbon holds two spins, which are forced to be parallel up-up spins (by red arrows in Fig. 2) or down-down spins (blue) for avoiding large coulomb repulsion due to Hund's rule[58)]. Spin alignment model is illustrated on middle. Three couples of spin-pair will be partially cancelled and remain one pair to be S_z=2/2. Such speculation is confirmed by DFT calculation. Spin cloud is mapped on right at a cutting surface of spin density at $10e/nm^3$. We can see up-spin major spin cloud coincident with above simple speculation.

As shown in panel of (C_{23}-a) in Fig. 1, molecular structure of S_z=0/2 shows bending top carbon (see a blue circle of side view), whereas S_z=2/2 shows flat one as illustrated on right column. It should be noted that stable spin state is S_z=2/2, not S_z=0/2. Molecular energy of S_z=2/2 was 0.49 eV lower (stable) than that of S_z=0/2. Cause of bending carbon of S_z=0/2 comes from partial inclusion of SP3 component among SP2 network[39)40)]. Such inclusion increases total molecular energy. Similar result was confirmed again for a case of (C_{23}-b).

Other molecules' structure and energy are listed in Fig. 1. Energy change from the spin state S_z=0/2 to the S_z=2/2 was noted by ΔE. Stable spin-state is framed by bold green. In most species, S_z=2/2 is stable (lower energy) than S_z=0/2. Exception is only (C_{53}-a) to show stable state of S_z=0/2. This comes from complete structure change, that is, void at a-site induces SP3-bond among SP2-networks as marked by a red circle in a column of (C_{53}-a, S_z=0/2).

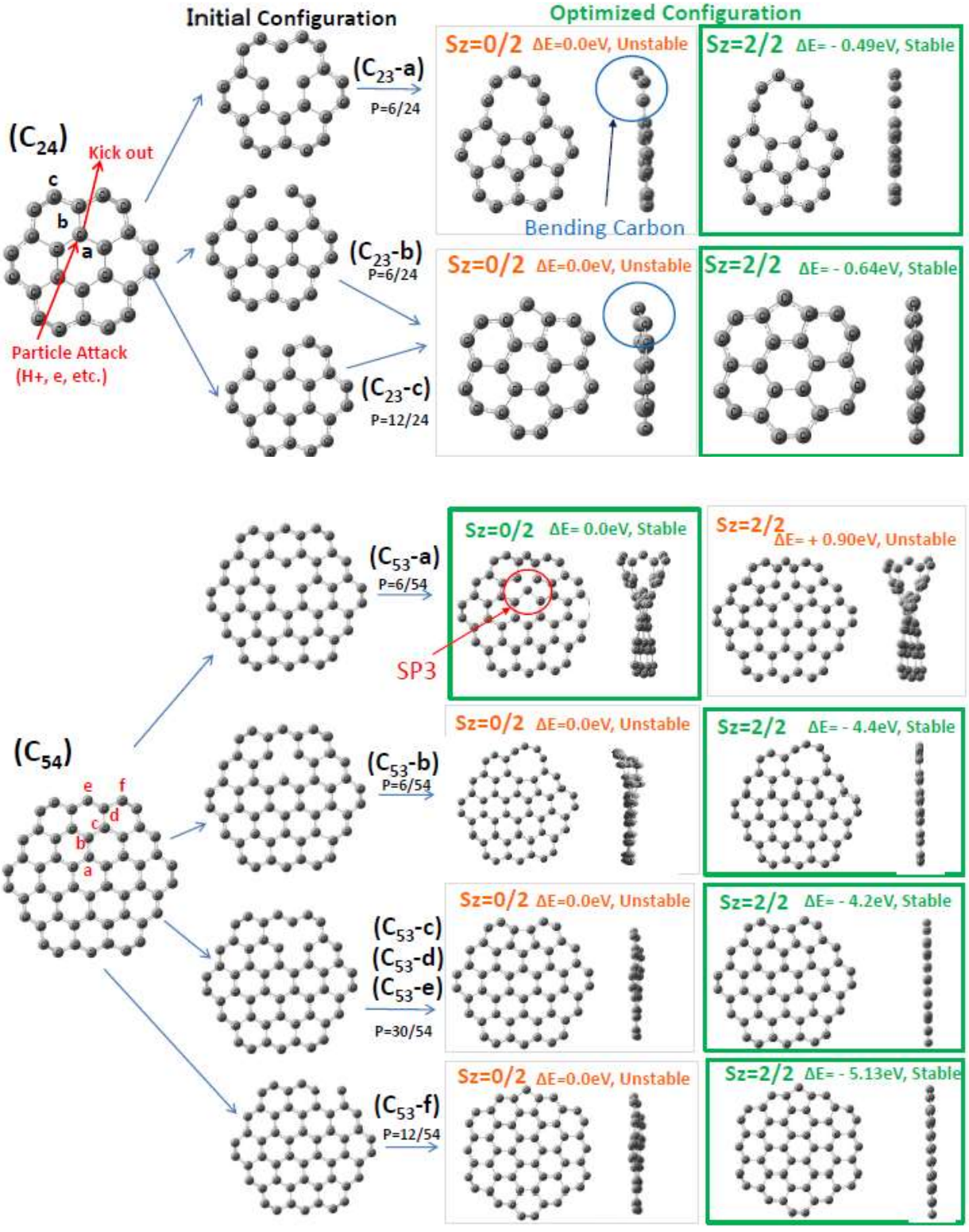

Fig. 1 Model graphene molecules. Void-defect positions are classified by suffix a, b, and so on. Calculated molecular structures are illustrated for both spin-states of S_z=0/2 and S_z=2/2. Total energy difference ΔE was noted in every column. Stable spin-state was framed by bold green.

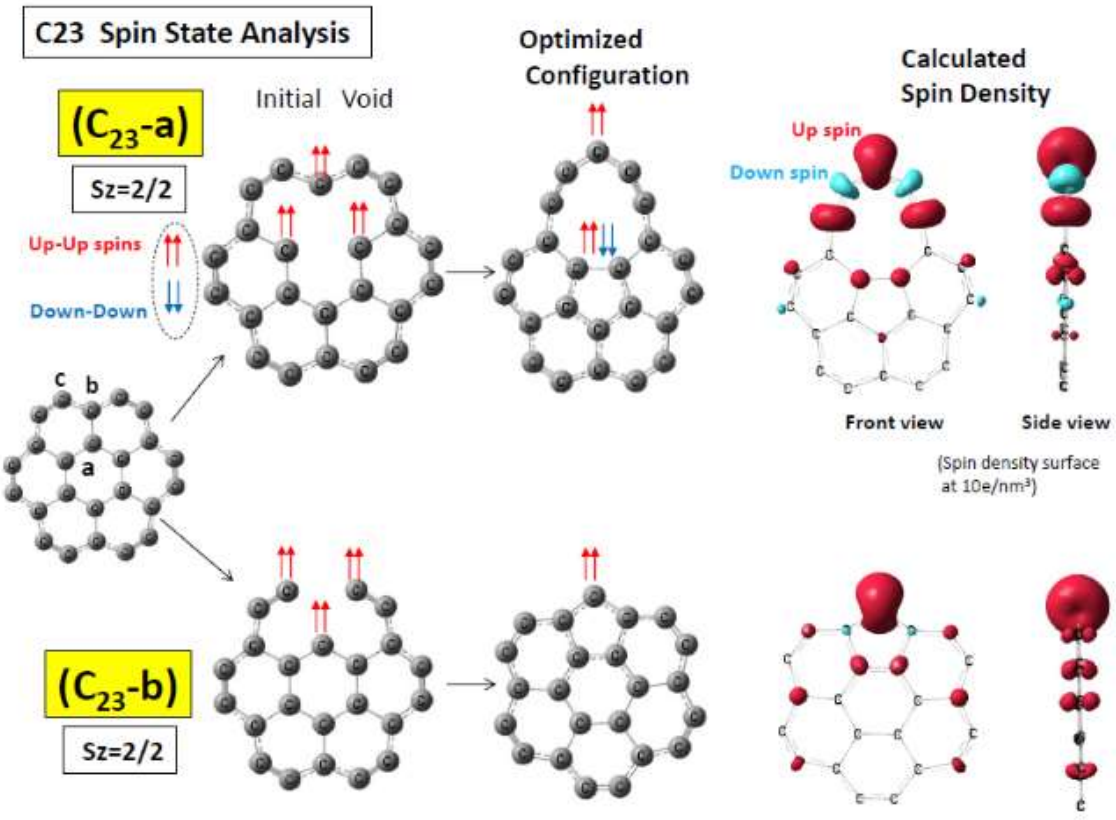

Fig. 2 Spin alignment for (C_{23}-a) and (C_{23}-b) with spin state of S_z=2/2. Initial void holds 3 radical carbons and allow 6 spins. By re-combination of carbon atoms, there arises partial cancelling of (up-up) spins by (down-down) one. DFT calculated spin density of S_z=2/2 is illustrated on right.

4. Calculated Infrared Spectrum

Calculated infrared spectra are shown in Fig. 3. Left columns are cases for spin state S_z=0/2, while right one S_z=2/2. Spectrum of stable spin state was framed by bold green. Astronomically observed major emission line of 18.9 μm was marked by a green dotted line. In case of (C_{23}-a), we can see one carbon pentagon ring and an unusual 9 membered ring. Calculated infrared spectrum for S_z=2/2 show 18.8 μm peak close to observed band of 18.9μm. The species of (C_{23}-b, S_z=2/2) [same structure for (C_{23}-c)] have one pentagon ring and show calculated twin major bands at 18.9 and 19.1 μm.

In case of (C_{53}-a), stable spin state was S_z=0/2, of which spectrum show peaks at 21.7 μm and 19.5 μm to be far from observed one. The spectrum of (C_{53}-b, S_z=2/2) show a peak at 19.0 μm close to observed one. Also, (C_{53}-c, S_z=2/2) [same for (C_{53}-d) and (C_{53}-e)] demonstrates major band at 18.9 μm, just the same with observed one. In case of (C_{53}-f, S_z=2/2), we can see twin bands at 18.4 and 18.9 μm. Thus, we could obtain several species suitable for assigning the astronomical observation.

5. Fundamental Mode Analysis

Fundamental vibrational mode of (C_{23}-b, S_z=2/2) was analyzed and summarized in Table 1. There are 63 modes for 23 carbon atoms. Energy diagram is illustrated on top right of Table 1. Zero-point vibrational energy is 27634 cm^{-1} (=3.42 eV). The lowest vibrational energy of Mode-1 is 94.9 cm^{-1} (=108.06 μm, 0.012 eV). The highest Mode-63 is 2067 cm^{-1} (=4.96 μm, 0.26 eV). Vibrational behaviors are noted on right column of the table. They are all carbon to carbon (C-C) in-plane stretching modes parallel to molecular plane. Combination of vibrating bonds is different for each mode. Bond is named by a, a', b, b' etc. illustrated on a molecule structure. For example, there are two calculated modes corresponding to observed 18.9 μm band. One is Mode-24 showing 18.8 μm in-plane C-C stretching at bonds of c, f, c', f', i, l, i' and l'. Another is Mode-23 showing 19.1 μm stretching at c, f, c', f', o, p, and o'. Other major modes will be discussed in next section by comparing astronomically observed bands.

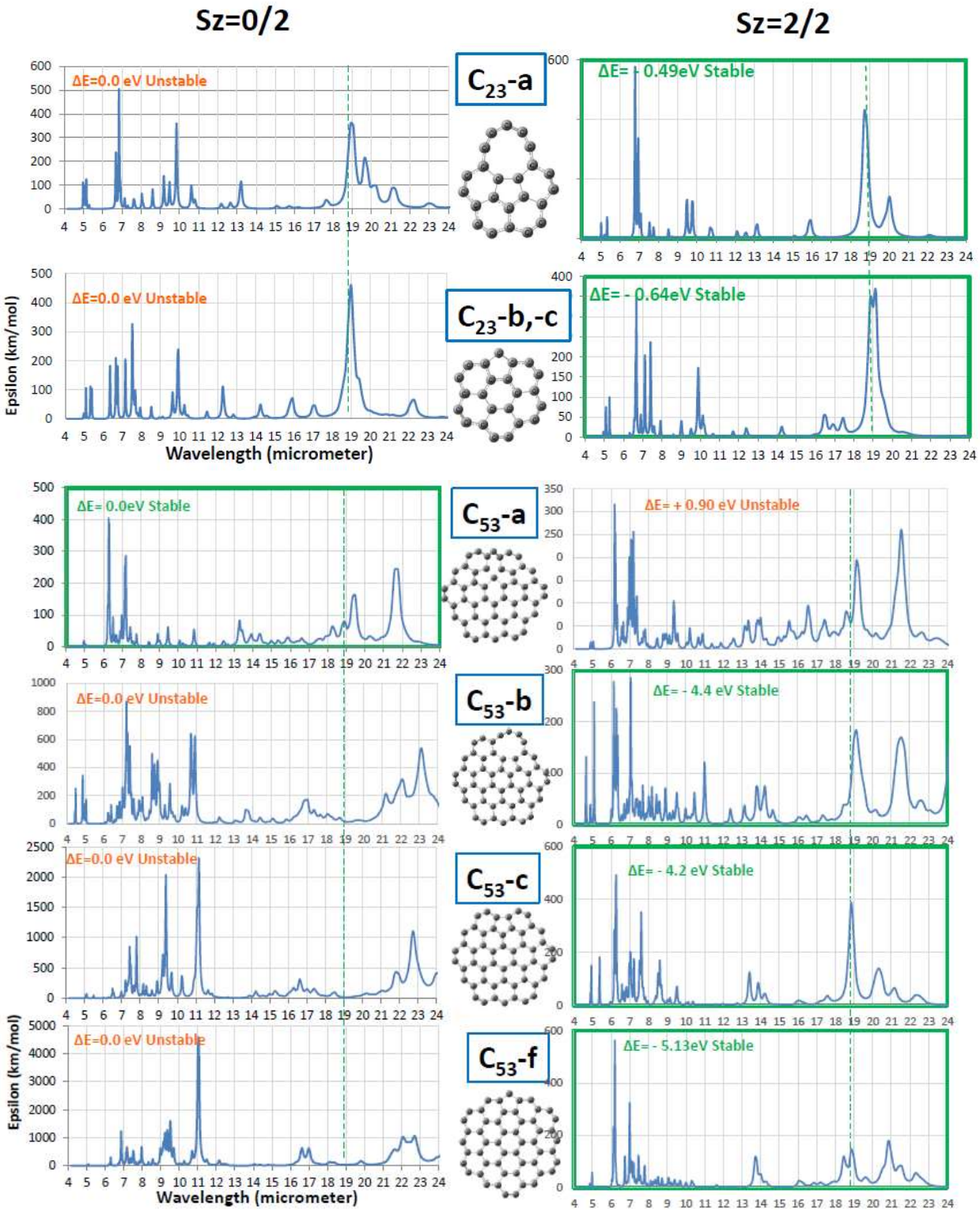

Fig. 3 Calculated infrared spectrum. Left figures are spectra for the spin state S_z=0/2, while right one for S_z=2/2. Stable spin state is framed by bold green.

Table 1 Fundamental mode analysis of (C_{23}, S_z=2/2).

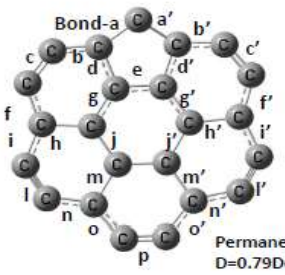

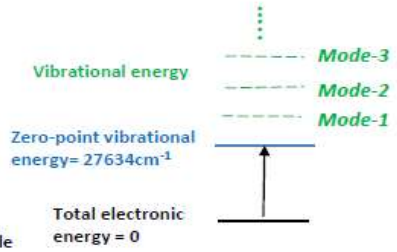

Astronomically Observed Band (μm)	Experimental Band (laser induced carbon plasma) (μm)	Fundamental Mode of (C23-b, Sz=2/2) , DFT calculation			
		Mode number	Wavelength (μm)	Intensity (km/mol)	Vibrational Behavior, Carbon to carbon in-plane stretching , bond positions
18.9μm		Mode-23 -24	19.1μm 18.8	92.6 78.8	c, f, c', f', i, l, i', l' c, f, c', f', o, p, a o'
17.4		-25	17.4	12.4	c, f, c', f'
16.7		-27	16.5	17.7	b, b', c, c'
10.0	10.2	-42	9.9	52.6	b, b', c, c'
7.5	7.4	-52	7.4	72.7	a, a, a', b, b', g, g', j, j'
7.0		-53	7.1	59.0	a, a', b, b', d, d', g, g', j, j', o, o'
6.6	6.7	-55 -56	6.7 6.6	94.0 40.5	a, a', b, b', f, f', i, i' n, n', o, o'

6. Comparison with Astronomical Observation

6.1 Single molecule spectrum

On top of Fig. 4, astronomically observed infrared spectra are illustrated for carbon rich planetary nebulae of Lin49 (dark blue curve) and Tc1 (red one). In both cases, we can see major band at 18.9 μm, also a side band at 17.4 μm, and shorter wavelength bands at 6.6, 7.0, 7.5, 8.1 and 8.5 μm. Sharp atomic emission lines are marked by arrows of [NeII] and [SIII] for scaling observed wavelength. It should be noted that the observed spectra are seen in emission. A nearby star as like a central star of Tc1 nebula may illuminate the molecules and excites them to give rise infrared emission. Detailed discussion was done by Li and Drain[48)49)]. We regard here that DFT calculated absorbed spectrum is mirror image of emission one in case of sufficient large photon energy excitation due to the theory of Einstein's emission coefficient[48),49)].

It was amazing to see good coincidence with observed spectra and calculated one of (C_{23}-b, S_z=2/2). Detailed comparison is summarized in Table 1. Observed major band at 18.9 μm could be identified by two modes of Mode-23 (19.1 μm) and Mode-24 (18.8 μm). Also, observed 6.6 μm band was reproduced well by calculated two modes of Mode-55 (6.7 μm) and Mode-56 (6.6 μm). Again, observed bands at 7.0, 7.5, 10.0, 16.7, and 17.4 μm could be reproduced well respectively by Mode-53 (for 7.1 μm), Mode-52 (7.4 μm), Mode-42 (9.9 μm), Mode-27 (16.5 μm), and Mode-25 (17.4 μm).

It was amazing again that large molecule cases as like (C_{53}-c, S_z=2/2) show good coincidence with observation as compared on a bottom panel of Fig. 4. It was suggested that there may be little size dependence. Void-defect induced graphene molecules generally contribute on cosmic spectra.

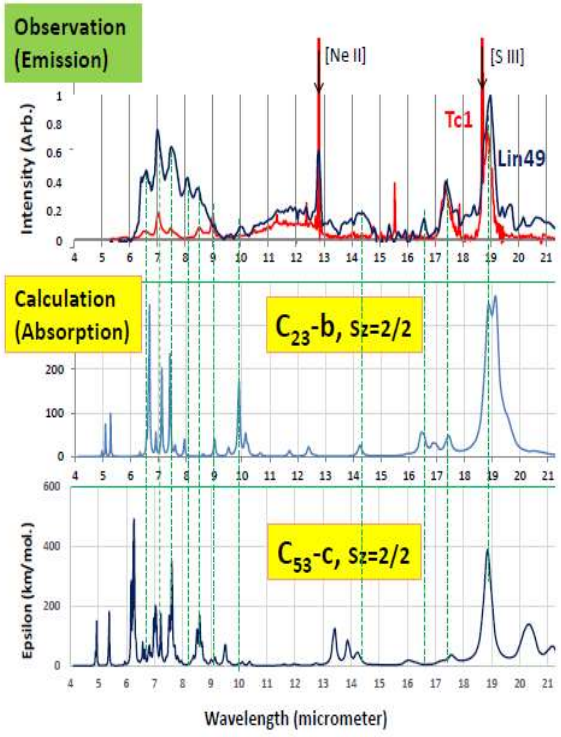

Fig. 4 Astronomically observed emission spectrum for planetary nebula Tc1 (on top, by red) and Lin49 (black) compared with calculated spectrum of (C_{23}-b, S_z=2/2), and (C_{53}-c, S_z=2/2).

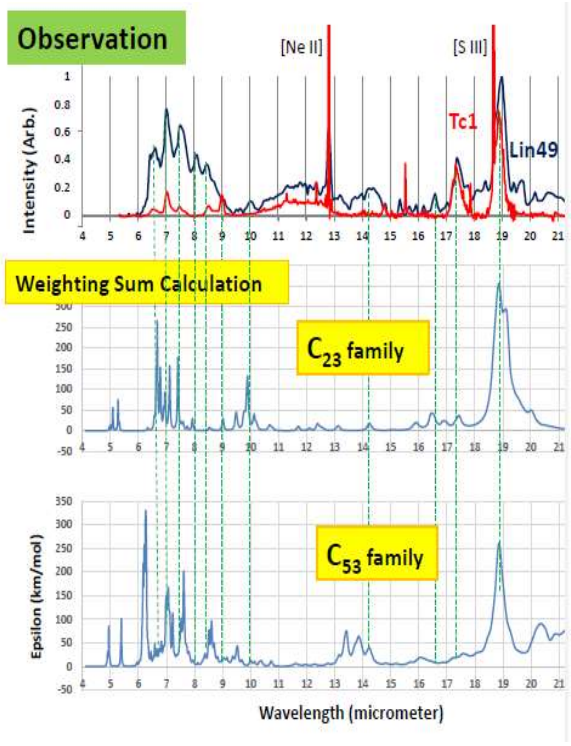

Fig. 5 Weighting sum spectra for C_{23}-family and C_{53}-family. Void creation capability parameter-p of each molecule is considered as weighting sum coefficient as noted in Fig. 1.

6.2 Weighting sum spectrum

We like to know total contribution of all model molecules, not depending on peculiar molecular species. Favorable way is the weighting sum method. In case of C_{23}-family, void-a species has 6 identical positions among 24 carbon sites of C_{24} mother molecule. Weighting sum coefficient-p should be p=6/24. Also, coefficient of void-b species is p'=6/24 and void-c p"=12/24. Weighting sum of epsilon ε(C_{23}-family) will be obtained by the following equation (1).

$$\begin{aligned}&\varepsilon(C_{23}\text{-family})\\&=p\cdot\varepsilon(C_{23}\text{-a}, S_z=2/2)+\\&\quad p'\cdot\varepsilon(C_{23}\text{-b}, S_z=2/2)+\\&\quad p''\cdot\varepsilon(C_{23}\text{-c}, S_z=2/2))\\&=(6/24)\cdot\varepsilon(C_{23}\text{-a}, S_z=2/2)+\\&\quad (6/24)\cdot\varepsilon(C_{23}\text{-b}, S_z=2/2)+\\&\quad (12/24)\cdot\varepsilon(C_{23}\text{-c}, S_z=2/2))\text{-------}(1)\end{aligned}$$

Weighting sum spectrum of C_{23}-family was illustrated on middle of Fig. 5. It was amazing that we can see good coincidence between observation and calculation. In case of larger molecule of C_{53}, weighting sum of C_{53}-family could well reproduce observed one as shown on bottom of Fig. 5, where void creation parameter p was noted in Fig. 1.

7. Comparison with Laboratory Experiment

Nemes et al.[41)42)] did the laser induced carbon plasma experiment as an analogy of carbon dust creation in interstellar space. Bulk graphite was heated and excited by Nd:YAG laser with wavelength of 1.064 μm (1.16 eV) in atmospheric pressure Argon gas. Evaporated carbon molecules emit infrared light. The emission was recorded by an HgCdTe detector.

Several theories dealt with the carbon dust creatin in space[50)-57)]. Calculated average size of carbon dust is about 1nm, which is similar size with C_{23} and C_{53} in this study. Temperature of star explosion gas will be 2000 K after 300 days of the explosion, and finally cooled as dust cloud[57)]. In case of laser induced plasma experiment, excited carbon temperature will be 4500 to 7000 K, and finally cooled to room temperature[42)].

Experimental spectrum is shown in panel (A) of Fig. 6. We compared with weighting sum spectrum of C_{23}-family and C_{53}-family in panel (B). The experimental 7.4 μm peak could be reproduced by calculated 7.5 μm band of C_{23}-family. We can see plateau from 6 to 7 μm, which may correspond to calculated bands at 6.7 and 7.2 μm. At a range of 5 μm, we can suggest some contribution by both C_{23}-family and C_{53}-family. Also, at a range of 10μm, C_{23}-family may contribute. It should be noted that void-defect

induced graphene could roughly explain laboratory experiment.

Comparison to astronomical observation was shown in panel (C). Astronomically observed bands are featured by black dotted lines. We can find again good reproducibility by calculation.

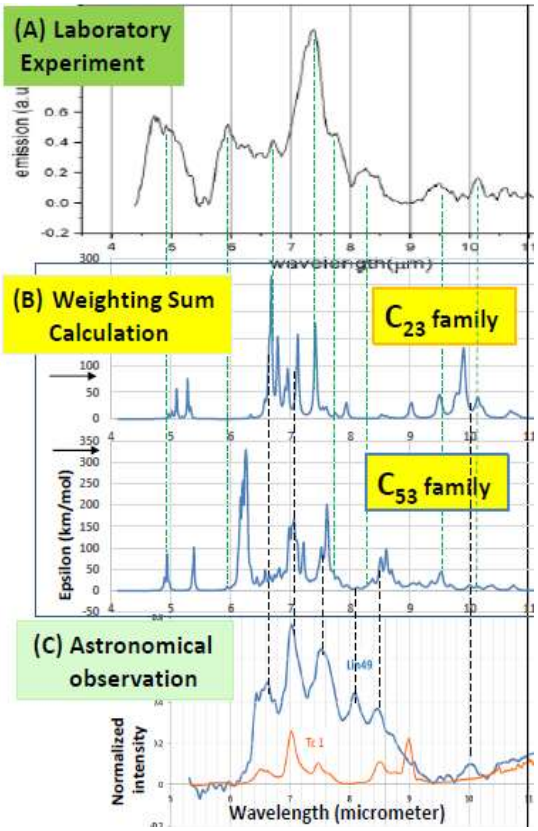

Fig. 6 (A) Infrared spectrum of the laser induced carbon plasma, (B) calculation for C_{23}-family and C_{53}-family, (C) astronomically observed spectra.

8. Conclusion

Void-defect is a possible origin of ferromagnetic like feature of graphene and graphite. In this paper, graphene molecules were studied.

(1) Starting model molecules were graphene molecules of C_{24} and C_{54} for the density functional theory analysis. Single void-defect creates C_{23}, and C_{53} having carbon pentagon ring among hexagon networks.

(2) Single void holds six spins to bring spin multiplicity. DFT calculation show the most stable spin-state to be S_z=2/2, not S_z=0/2.

(3) We compared calculated infrared spectrum with astronomically observed one. Interstellar carbon is expected to avoid complex molecule-to-molecule interaction. The triplet spin state of C_{23} and C_{53} could explain astronomically observed spectra of Tc1 and Lin49 nebulae for a major band at 18.9μm and sub-bands from 6 to 18μm.

(4) By a weighting sum method applied to different void position species, again we could reproduce well observed infrared spectra.

(5) The laboratory experiment on laser induced carbon plasma was tried as an analogy for carbon dust creation in space. Experimental infrared emission spectra could be roughly explained by the weighting sum spectra of C_{23} and C_{53}.

Acknowledgement

Aigen Li is supported in part by NSF AST-1311804 and NASA NNX14AF68G.

References

(Note on abbreviation of astronomical journals,
ApJ: The Astrophysical Journal
ApJL: The Astrophysical Journal Letters
A&A: Astronomy and Astrophysics
MNRAS: Monthly Notices of the Royal Astronomical Society
PNAS: Proceedings of the National Academy of Sciences)

1) P. Esquinazi, D. Spemann, R. Hohne, A.Setzer, K. Han, and T. Butz: *Phys. Rev. Lett.*, **91**, 227201 (2003).
2) K. Kamishima, T. Noda, F. Kadonome, K. Kakizaki and N. Hiratsuka: *J. Mag. Magn. Mat.*, **310**, e346 (2007).
3) T. Saito, D. Nishio-Hamane, S. Yoshii, and T. Nojima: *Appl. Phys. Lett.*, **98**, 052506 (2011).
4) Y. Wang, Y. Huang, Y. Song, X. Zhang, Y. Ma, J. Liang and Y. Chen: *Nano Letters* , **9,** 220 (2009).
5) J. Cervenka, M. Katsnelson and C. Flipse: *Nature Phys.*, **5**, 840 (2009), (https://doi.org/10.1038/nphys1399) .
6) H. Ohldag, P. Esquinazi, E. Arenholz, D. Spemann, M. Rothermal, A. Setzer, and T. Butz: *New Journal of Physics*, **12**, 123012 (2010).
7) J. Coey, M. Venkatesan, C. Fitzgerald, A. Douvalis and I. Sanders: *Nature*, **420**, 156 (2002).
8) K. Kusakabe and M. Maruyama: *Phys. Rev. B*, **67**, 092406 (2003).
9) N. Ota, N. Gorjizadeh and Y. Kawazoe: *J. Magn. Soc. Jpn.*, **35**, 414 (2011), also **36**, 36 (2012).
10) N. Ota: *J. Magn. Soc. Jpn.*, **37**, 175 (2013).
11) P. Lehtinen, A. Foster, Y. Ma, A. Krasheninnikov, and R. Nieminen: *Phys. Rev. Lett.* , **93**, 187202 (2004).
12) P.Ruffieux, O. Groning, P. Schwaller, L. Schlapbach, and P. Groning: *Phys. Rev. Lett.,* **84,** 4910 (2000).
13) A. Hashimoto, K. Suenaga, T. Sugai, H.Shinohara, and S. Iijima: *Nature (London),* **430**, 870 (2004).
14) K.Kelly and N.Hales: *Sur. Sci.*, **416**, L1085 (1998).
15) T. Kondo, Y. Honma, J. Oh, T. Machida, and J. Nakamura: *Phys. Rev. B*, **82**, 153414 (2010).
16) M. Ziatdinov, S. Fujii, K. Kusakabe, M. Kiguchi, T. Mori, and T. Enoki: *Phys. Rev. B*, ***89***, 155405 (2014).
17) K.Kelly and N.Hales: *Sur. Sci.,* **416**, L1085 (1998).
18) T. Kondo, Y. Honma, J. Oh, T. Machida, and J. Nakamura: *Phys. Rev. B*, **82**, 153414 (2010).

19) M. Ziatdinov, S. Fujii, K. Kusakabe, M. Kiguchi, T. Mori, and T. Enoki: *Phys. Rev. B*, **89,** 155405 (2014).
20) O. Yazyev and L. Helm: *Phys. Rev. B,* **75**, 125408 (2007).
21) B. Wang and S. Pantelides: *Phys. Rev. B*, **86**, 165438 (2012).
22) H. W. Kroto, J. R. Heath, S. C. Obrien, R. F. Curl, and R. E. Smalley: *Nature*, **318**, 162 (1985).
23) J. Cami, J. Bernard-Salas, E. Peeters and S. E. Malek: *Science,* **329**, 1180 (2010).
24) K. Sellgren, M. W. Werner, J. G. Ingalls, J. D. T. Smith, T. M. Carleton and J. Christine: *ApJL,* **722**, L54 (2010).
25) Y. Zhang, & S. Kwok: *ApJ*, **730**, 126 (2011).
26) O. Bern´e & A. G. G. M.Tielens: *PNAS*, **109,** 4010 (2012) Also, Bern´e, N. L. J. Cox, G. Mulas & C. Joblin: *A&A,* **605**, L1 (2017).
27) D. A. Garc´ıa-Hern´andez, A. Manchado, P. Garc´ıa-Lario, et al.: *ApJL,* **724**, L39 (2010).
28) M. Otsuka, F. Kemper, M. L. Leal-Ferreira, M. L. Aleman, M. L. Bernard-Salas, J. Cami, B. Ochsendorf, E. Peeters, and P. Scicluna: *MNRAS*, **462,** 12 (2016).
29) M. C. Martin, D. Koller, and L. Mihaly: Phys. Rev. **B47**, 14607 (1993).
30) J. Fabian: *Phys. Rev.* **B53**, 13864 (1996).
31) A. Candian, M. G. Rachid, H. MacIssac, V. N. Staroverov, E. Peeters, and J. Cami: preprint from web site of *ResearchGate* by Allessandra Candians, titled "Searching for stable fullerenes in space with computational chemistry" (2009).
32) H.W. Kroto & K. McKay: *Nature*, **331**, 328 (1988).
33) A. Chuvilin, U. Kaiser, E. Bichoutskaia, N. A. Besley, & A.N. Khlobystov: *Nature Chem.*, **2**, 450 (2010).
34) A. K. Geim & K. S. Novoselov: *Nature Materials,* **6**, 183 (2007).
35) D. A. Garcıa-Hernandez, Rao N. Kameswara & D. L. Lambert: *ApJ*, **729**, 126 (2011).
36) D. A. Garcıa-Hernandez, S. Iglesias, J. A. Acosta-Pulido, et al.: *ApJL*, **737,** L30 (2011).
37) D. A. Garcıa-Hernandez, E. Villaver, P. Garc´ıa-Lario, et al.: *ApJ*, **760**, 107 (2012).
38) C. Duboscq, F. Caldvo, M. Rapacioli, E. Dartois, T. Pino, C. Falvo, and A. Simon: *A& A,* **634,** A62 (2020).
39) N. Ota: *arXiv,* 1412.0009 (2014), Additional data for scaling factor on *arXiv,* 1502.01766,
for emission spectrum calculation on *arXiv,* 1703.05931,
for SP3 defect mechanism on *arXiv,* 1808.01070.
40) H. Galue, and G. Leines: *Phys. Rev. Lett.,* **119**, 171102 (2017).
41) L. Nemes, A. Keszler, J. Hornkohl, and C. Parigger: *Applied Optics*, **44-18**, 3661 (2005).
42) L. Nemes, E. Brown, S. C. Yang, U. *Hommerrich: Spectrochimica Acta Part A, Molecular and Biomolecular Spectroscopy,* **170**, 145 (2017).
43) P. Hohenberg and W. Kohn: *Phys. Rev.*, **136**, B864 (1964).
44) W. Kohn and L. Sham: *Phys. Rev.*, **140**, A1133 (1965).
45) A. Becke: *J. Chem. Phys.*, **98**, 5648 (1993).
46) M. Frisch, G. Trucks, H. Schlegel et al: Gaussian 09 package software, Gaussian Inc. Wallington CT USA (2009).
47) R. Ditchfield, W. Hehre and J. Pople: *J. Chem. Phys.,* **54**,724(1971).
48) B. T. Draine and A. Li: *ApJ,* **551**, 807 (2001).
49) A. Li and B. T. Draine: *ApJ,* **554**, 778 (2001).
50) T. Nozawa, T. Kozasa, H. Umeda, K. Maeda & K. Nomoto: *ApJ,* **598**, 785 (2003).
51) T. Kozasa and H. Hasegawa: *Prog. Theor. Phys.,* **77**, 1402 (1987).
52) T Kozasa T., et al.: *ASP Conf. Ser.* **414**, *Cosmic Dust-Near and Far,* p-43 (2009).
53) T. Nozawa, T. Kozasa, A. Habe: *ApJ ,* **648,** 435 (2006).
54) X. H. Chen, A. Li, & K. Zhang: *ApJ,* ,**850**, 104 (2017).
55) N. Ota: *arXiv,* 1803.09035 (2018), Additional data on *arXiv,* 1811.05043 (2018).
56) Q. Li, A. Li & B. W. Jiang: MNRAS, in press also in *arXiv,* 1909.12210 (2019).
57) T. Nozawa, T. Kozasa, N. Tominaga, H. Umeda, K. Maeda, K. Nomoto, and O. Krause: *ApJ*, **713**, 356 (2010).
58) F. Hund: *Z. Phys.* **33**, 345 (1923).

Received Oct. 25, 2020; Accepted Jan. 21, 2021.

Journal of the Magnetics Society of Japan

Vol. 45 No. 2 (通巻第314号) 2021年3月1日発行

Vol. 45 No. 2 Published Mar. 1, 2021
by the Magnetics Society of Japan
Tokyo YWCA building Rm207, 1–8–11 Kanda surugadai, Chiyoda-ku, Tokyo 101–0062
Tel. +81–3–5281–0106 Fax. +81–3–5281–0107

Printed by JP Corporation Co., Ltd.
Sports Plaza building 401, 2–4–3, Shinkamata Ota-ku, Tokyo 144–0054
Advertising agency: Kagaku Gijutsu-sha

発行：（公社）日本磁気学会 101–0062 東京都千代田区神田駿河台 1–8–11 東京YWCA会館 207 号室
製作：ジェイピーシー 144–0054 東京都大田区新蒲田 2–4–3 スポーツプラザビル401 Tel.（03）6715–7915
広告取扱い：科学技術社 111–0052 東京都台東区柳橋 2–10–8 武田ビル4F Tel.（03）5809–1132